

1 **Markedly different impacts of primary emissions and secondary**
2 **aerosol formation on aerosol mixing states revealed by simultaneous**
3 **measurements of CCNC, V/HTDMA, and SP2**

4 Jiangchuan Tao^{1,8}, Biao Luo^{1,8}, Weiqi Xu³, Gang Zhao⁶, Hanbin Xu⁵, Biao Xue^{1,8}, Miaomiao Zhai^{1,8},
5 Wanyun Xu⁴, Huarong Zhao⁷, Sanxue Ren⁷, Guangsheng Zhou⁷, Li Liu^{2,*}, Ye Kuang^{1,8,*}, Yele Sun³

6 ¹ Institute for Environmental and Climate Research, Jinan University, Guangzhou, Guangdong, China

7 ² Key Laboratory of Regional Numerical Weather Prediction, Institute of Tropical and Marine
8 Meteorology, China Meteorological Administration, Guangzhou, China.

9 ³ State Key Laboratory of Atmospheric Boundary Layer Physics and Atmospheric Chemistry, Institute
10 of Atmospheric Physics, Chinese Academy of Sciences, Beijing, China.

11 ⁴ State Key Laboratory of Severe Weather, Key Laboratory for Atmospheric Chemistry, Institute of
12 Atmospheric Composition, Chinese Academy of Meteorological Sciences, Beijing, China

13 ⁵ Experimental Teaching Center, Sun Yat-Sen University, Guangzhou, China

14 ⁶ State Key Joint Laboratory of Environmental Simulation and Pollution Control, International Joint
15 Laboratory for Regional Pollution Control, Ministry of Education, College of Environmental Sciences
16 and Engineering, Peking University, Beijing 100871, China

17 ⁷ Hebei Gucheng Agricultural Meteorology National Observation and Research Station, Chinese
18 Academy of Meteorological Sciences, Beijing, 100081, China

19 ⁸ Guangdong-Hongkong-Macau Joint Laboratory of Collaborative Innovation for Environmental
20 Quality, Jinan University, Guangzhou, Guangdong, China

21 Correspondence: Ye Kuang (kuangye@jnu.edu.cn), Li Liu (liul@gd121.cn)

22

23 **Abstract**

24 This study compares aerosol mixing state parameters obtained via simultaneous measurements using
25 DMA-CCNC, H/V-TDMA, and DMA-SP2, shedding light on the impacts of primary aerosol
26 emissions and secondary aerosol (SA) formation. The analysis reveals significant variations in mixing-
27 state parameters among different techniques, with V-TDMA and DMA-SP2 indicating that non-
28 volatile particles mainly stem from BC-containing aerosols, while a substantial proportion of nearly
29 hydrophobic aerosols originates from fossil fuel combustion and biomass burning emissions.
30 Synthesizing the results, some nearly hydrophobic BC-free particles were found to be CCN-inactive
31 under the measured supersaturated conditions, likely from fossil fuel combustion emissions, while
32 others were CCN-active, linked to biomass burning emissions. Moreover, BC-containing aerosols
33 emitted from fossil fuel combustion exhibit more external mixing with other aerosol components
34 compared to those from biomass burning. Secondary nitrate and organic aerosol formation
35 significantly affect aerosol mixing states, enhancing aerosol hygroscopicity and volatility while
36 reducing heterogeneity among techniques. The study also highlights distinct physical properties of two
37 resolved secondary organic aerosol factors, hinting at formation through different mechanisms. These
38 findings underscore the importance of comparing aerosol mixing states from different techniques as a
39 tool in understanding aerosol physical properties from different sources and their responses to SA
40 formation, as well as aiding in the exploration of SA formation mechanisms.

41 **1 Introduction**

42 The aerosol mixing state is a crucial physicochemical property of aerosol particles (Riemer et al.,
43 2019), exerting a significant impact on their optical properties and cloud condensation nuclei (CCN)
44 activity, thus affecting their impact on the climate and environment (Fierce et al., 2017; Riemer et al.,
45 2019; Stevens et al., 2022). For example, variations in the mixing state of black carbon (BC) particles
46 can significantly alter their absorption and radiative effects (Bond et al., 2013; Lack et al., 2012; Zhao
47 et al., 2019; Moffet et al., 2016; Matsui et al., 2018; Peng et al., 2016). Using simple internal mixing
48 state assumptions for aerosol chemical components to estimate CCN number concentrations can lead
49 to substantial overestimations (up to 30%; Deng et al., 2013; Farmer et al., 2015; Ren et al., 2018;
50 Ching et al., 2017, 2019; Tao et al., 2021). The aerosol mixing state varies widely due to complex
51 emissions and atmospheric transformations, leading to significant uncertainties in estimating the
52 effects of aerosols based on simplified mixing state assumptions (Ervens, 2015; Wang et al., 2022; Fu
53 et al., 2022).

54 The aerosol mixing state describes the mixture of aerosol chemical components within each
55 particle and the distribution of these particles in the aerosol population. This property can be directly
56 measured using single-particle chemical composition techniques (Fierce et al., 2017; Riemer et al.,
57 2019), such as the single-particle soot photometer (SP2), which measures refractory black carbon (rBC)
58 mass concentrations and the mixing state of rBC with other aerosol components, or single-particle
59 chemical composition measurement techniques (e.g., single-particle aerosol mass spectrometer, SP-
60 AMS) that have been developed in recent years (Lee et al., 2019; Riemer et al., 2019 and reference
61 therein). Alternatively, the aerosol mixing state can be inferred from indirect measurements of aerosol
62 properties, such as size-resolved aerosol CCN activity (measured by coupling a differential mobility
63 analyzer (DMA) and a CCN counter (CCNC)), size-resolved aerosol hygroscopicity distributions, or
64 volatility distributions (measured by a Humidified/Volatility Tandem differential mobility analyzer
65 (H/V-TDMA)).

66 However, each technique yields information on aerosol mixing states based on different aerosol
67 microphysical properties, thus obtaining aerosol mixing states that are different but linked to one
68 another. For instance, while both CCN activity and hygroscopic growth measurements are associated
69 with aerosol hygroscopicity, an intercomparison between CCNC and HTDMA measurements has

70 prompted investigations into aerosol hygroscopicity variations under different saturation conditions
71 (Su et al., 2010; Juranyi et al., 2013; Lance et al., 2013; Kawana et al., 2016; Tao et al., 2020; Jiang et
72 al., 2021). Although the SP2 and VTDMA techniques depend on the evaporation of non-refractory
73 compositions, only rBC remains in the SP2 measurements. In contrast, non-refractory composition
74 evaporation depends on the thermodynamic temperature in the VTDMA measurements. Thus,
75 measurements of an SP2 are highly correlated to those of a VTDMA at high temperatures (200 °C–
76 300 °C), with their differences reflecting variations in aerosol density, shape, or volatility (Philippin
77 et al., 2004; Wehner et al., 2009; Adachi et al., 2018, 2019; Wang et al., 2022). HTDMA and VTDMA
78 can be combined to study the influence of the aerosol mixing state on hygroscopicity and volatility
79 (Zhang et al., 2016; Cai et al., 2017; Wang et al., 2017). Strong correlations were found between the
80 hydrophobic and non-volatile particles, suggesting they might have similar chemical compositions
81 (Zhang et al., 2016). In addition, some studies have shown that, except for BC, low-volatility particles
82 correlate well with CCN-inactive particles based on VTDMA and CCNC measurements (Kuwata et
83 al., 2007; Kuwata and Kondo, 2008; Rose et al., 2011; Cheng et al., 2012). Therefore,
84 intercomparisons between mixing state parameters measured by distinct techniques provide a better
85 characterization of the aerosol mixing state and insight into aerosol physiochemical properties.
86 Previous studies have mainly compared two types of aerosol mixing state measurements and lacked a
87 comprehensive comparative analysis among SP2, DMA-CCN, and HV-TDMA measurements,
88 hindering the wide application of derived aerosol mixing states obtained by individual techniques.

89 The mixing state of primary aerosols can vary greatly depending on their type and emission
90 conditions (Cheng et al., 2012; Wang et al., 2017; Wang et al., 2022; Ting et al., 2018; Liu et al., 2021)
91 and can be significantly altered during aging processes or secondary formation (Wehner et al., 2009;
92 Cheng et al., 2012; Wang et al., 2022; Tomlin et al., 2021; Lata et al., 2021). Primary aerosol emissions,
93 such as biomass burning, fossil fuel combustion, and cooking, tend to contribute to weak
94 hygroscopicity (Herich et al., 2008, 2009; Wang et al., 2020; Kim et al., 2020) and low-volatility
95 aerosols (Hong et al., 2017; Saha et al., 2018). The formation of secondary aerosols (SAs), including
96 the aging of BC-containing particles and primary organic aerosols, mainly contributes to aerosols with
97 strong CCN activity (Mei et al., 2013; Ma et al., 2016; Tao et al., 2021) and high hygroscopicity (Chen
98 et al., 2018; Kim et al., 2020; Wang et al., 2020). It is important to study the impact of specific primary

99 aerosol emissions and SA formation on aerosol mixing states and the influence of aerosol mixing state
100 parameters derived from different techniques to enhance our understanding of the mixing state of
101 aerosols from different emission sources and improve their characterization in models.

102 The North China Plain (NCP) is among the most polluted regions in China, with various primary
103 emission sources and strong SA formations that play critical roles in air pollution (Xu et al., 2011; Tao
104 et al., 2012; Liu et al., 2015). The complex mixing state of aerosols in the NCP contributes to
105 uncertainties in evaluating their climate and environmental effects (Zhuang et al., 2013; Nordmann et
106 al., 2014; Zhang et al., 2016; Tao et al., 2020; Shi et al., 2022), particularly regarding BC particles
107 (Wu et al., 2017; Liu et al., 2019; Zhao et al., 2019; Wang et al., 2011; Zheng et al., 2019).
108 Meteorological conditions can greatly affect SA formation in the NCP and can be significantly
109 exacerbated during severe pollution events. SA formation under low relative humidity (RH) conditions,
110 mainly through the condensation of gaseous-phase oxidation products, would change to that mainly
111 occurring in the aqueous phase under high RH conditions (Kuang et al., 2020). Because SAs formed
112 through different mechanisms, have different chemical compositions and add mass to different aerosol
113 populations, SA formation under different meteorological conditions can affect the aerosol mixing
114 states differently (Tao et al., 2021). This study obtained the aerosol mixing state through concurrent
115 measurements of the CCN activity, hygroscopicity, volatility, and BC particles at a regional site in the
116 NCP using CCNC, HTDMA, VTDMA, and SP2 instruments. This provides a unique opportunity to
117 perform a comprehensive inter-comparison of the aerosol mixing states among different techniques to
118 gain insight into the impact of primary aerosol emissions and SA formation on the observed aerosol
119 mixing states.

120

121 **2 Materials and methods**

122 **2.1 Campaign information and instruments setup**

123 From the 16th of October to the 16th of November 2021, aerosol mixing states were continuously
124 and concurrently monitored using different techniques at the Gucheng site in Dingxing County, Hebei
125 Province, China, as part of a campaign to investigate AQueous Secondary aerOsol Formation in Fog
126 and Aerosols and their Radiative effects in the NCP (AQ-SOFAR). The observation site, located at
127 39°09'N, 115°44'E, is an Ecological and Agricultural Meteorology Station of the Chinese Academy

128 of Meteorological Sciences, situated between the megacities of Beijing (approximately 100 km away)
129 and Baoding (approximately 40 km away) and surrounded by farmlands and small towns. This site
130 provides a representative view of the background atmospheric pollution conditions in the NCP (Kuang
131 et al., 2020; Li et al., 2021).

132 Different measurement techniques were used to simultaneously obtain the aerosol mixing state
133 through CCN activity, hygroscopicity, volatility, and BC particle observations. In addition to aerosol
134 mixing state measurements, the AQ-SOFAR campaign includes measurements of aerosol number size
135 distribution, chemical composition, aerosol scattering, and absorption properties. Aerosol number size
136 distributions in the diameter range of 13 nm–4 μm were measured by the scanning mobility particle
137 sizer (13–550 nm) and the aerodynamic aerosol classifier (100 nm–4 μm), and they are merged by
138 assuming an aerosol density of 1.6 g/cm^3 . The total BC mass concentrations were determined using an
139 aethalometer (Magee, AE33; Drinovec et al., 2015); more information on the correction of absorption
140 measurements and mass concentration calculations is available in Luo et al. (2022). All aerosol
141 measurement instruments were housed in a temperature-controlled container at 24 $^{\circ}\text{C}$. The inlet was
142 switched among three impactors: TSP (Total Suspended Particles), $\text{PM}_{2.5}$ (Particulate Matter with an
143 aerodynamic diameter of less than 2.5 μm), and PM_1 (Particulate Matter with an aerodynamic diameter
144 of less than 1 μm). Inlet changes among impactors affect dry-state aerosol sampling owing to ambient
145 aerosols are enlarged through aerosol hygroscopic growth or activation. However, the aerosol mixing
146 state and aerosol chemical composition measurements were made on submicron aerosols, and the inlet
147 change almost did not affect those measurements under conditions of RH less than 90%. The sampled
148 aerosol was dried by two parallelly assembled Nafion dryers with a length of 1.2 m. Two Nafion driers
149 used because of the high RH and sample flow rate ($\sim 16 \text{ L}/\text{min}$) during the campaign to ensure drying
150 efficiency. The flow rate is carefully adjusted in the inlet in order to ensure accurate aerosol particle
151 size cutoff. In addition, during autumn and winter in the NCP, ambient air temperature ($<20 \text{ }^{\circ}\text{C}$ and
152 sometimes $<0 \text{ }^{\circ}\text{C}$) can be significantly lower than the room temperature ($\sim 24 \text{ }^{\circ}\text{C}$). Therefore, this dryer
153 system can maintain the RH of sampled aerosols to below 20%. Meteorological data such as
154 temperature, pressure, wind speed, wind direction, and RH were obtained from an automatic weather
155 station operated by the station.

156 The chemical composition of the submicron aerosols was analyzed using a High-Resolution
157 Time-of-Flight Aerosol Mass Spectrometer (HR-ToF-AMS). The ionization efficiency (IE) was

158 calibrated using 300 nm diameter pure NH_4NO_3 particles, following the standard protocols outlined in
159 Jayne et al. (2000) in the middle of the campaign, with the relative ionization efficiency (RIE) of
160 ammonium determined to be 5.26. The RIE of sulfate was 1.28 using pure $(\text{NH}_4)_2\text{SO}_4$ particles, and
161 the default RIEs of 1.4 for organic aerosols, 1.1 for nitrates, and 1.3 for chlorides were used as the
162 organic aerosols. The composition-dependent collection efficiency reported by Middlebrook et al.
163 (2012) was used. Elemental ratios were derived using the “Improved-Ambient (I-A)” method as
164 described in Canagaratna et al. (2015), including hydrogen to carbon (H/C), oxygen to carbon (O/C),
165 and organic mass to organic carbon (OM/OC) ratios. Two primary organic aerosol (POA) and two
166 oxygenated organic aerosol (OOA) factors were identified by High-Resolution Positive Matrix
167 Factorization (HR-PMF; Ulbrich et al., 2009; Paatero and Tapper, 1994). This study used the
168 summation of the two OOA factors to represent secondary organic aerosols (SOA). The mass spectra
169 of the organic aerosol (OA) factors and their correlations with external species are shown in Figs. S1
170 and S2. The Biomass Burning Organic Aerosol (BBOA) spectrum was characterized by abundant
171 fragments of m/z 60 (mainly $\text{C}_2\text{H}_4\text{O}_2^+$) and 73 (mainly $\text{C}_3\text{H}_5\text{O}_2^+$), two indicators of biomass burning
172 (Mohr et al., 2009). BBOA correlated well with $\text{C}_2\text{H}_4\text{O}_2^+$ ($R^2=0.91$) and $\text{C}_3\text{H}_5\text{O}_2^+$ ($R^2=0.90$). Consistent
173 with previous studies in Beijing (Xu et al., 2019), the PMF analysis revealed a mixed factor named
174 Fossil Fuel Organic Aerosol (FFOA), which comprises traffic emissions and coal combustion and is
175 characterized by a typical hydrocarbon ion series. FFOA had a relatively high f_{44} (0.083) value, which
176 was likely due to aging during regional transportation, similar to the results observed in the winter of
177 2016 in Beijing (Xu et al., 2019) and coal combustion organic aerosols in Gucheng (Chen et al., 2022).
178 Secondary organic aerosol formation from volatile organic compound precursors could occur in
179 different formation pathways, such as aqueous-phase, heterogeneous, or gas-phase reactions. It might
180 also be oxidized under different conditions, such as oxidation under different nitrogen oxide conditions
181 with different oxidation capacities and oxidants. The two resolved OOA factors displayed different
182 spectral patterns, correlations with tracers, and diurnal variations, suggesting that they resulted from
183 different chemical processes. However, their formation mechanisms remain to be explored in future
184 studies. In general, the OOA factor 1 (OOA1) has higher $\text{CO}_2^+/\text{C}_2\text{H}_3\text{O}^+$ (3.9) and O/C (0.91) ratios
185 than OOA factor 2 (OOA2) with 2.1 and 0.78, respectively. The mass fraction (MF) of each chemical
186 composition is calculated as the bulk mass fraction of each chemical composition in non-refractory
187 PM_{10} (NR- PM_{10}).

188 This study did not consider losses in the inlet line and sampling systems for the following
189 reasons: (1) investigated mixing state parameters are represented by number fractions (NFs) of
190 different diameters, which are much less affected by losses in sampling systems compared with
191 absolute number concentrations; and (2) good consistency was achieved between measurements of
192 particle number size distributions (PNSD) and mass concentrations measured by AMS. The average
193 ratio between volume concentration derived from AMS and rBC measurements (densities of
194 compounds are the same as Kuang et al., 2021) and the volume concentration derived from PNSD
195 measurements was 0.79 ($R=0.97$, as shown in Fig. S3), consistent with previous reports as AMS cannot
196 detect aerosol components, such as dust (Kuang et al., 2021).

197 **2.2 Aerosol mixing states measurement techniques**

198 **2.2.1 DMA-CCNC measurements**

199 The CCN activity of the particles under supersaturated conditions was measured using a DMA-
200 CCNC system, which consisted of a differential mobility analyzer (DMA; model 3081, TSI, Inc., MN,
201 USA), condensation particle counter (CPC; model 3756, TSI, Inc., MN, USA), and continuous-flow
202 CCNC (model CCN100, Droplet Measurement Technologies, USA). The system was operated in size-
203 scanning mode and provided the Size-resolved Particle Activation Ratio (SPAR) by combining CPC
204 and CCNC measurements at different particle sizes. To compare the instruments, three
205 supersaturations (SSs) of 0.08%, 0.14%, and 0.22% were applied in a single cycle of approximately
206 15 min. CCN measurements under these three SSs revealed that the CCN activity of aerosols resides
207 in the accumulation mode with an aerosol diameter range of approximately 100–200 nm, which is
208 close to the diameters of the HV-TDMA measurements. Higher SSs would reveal CCN activities of
209 smaller aerosol particles (<100 nm), where the DMA-SP2 measurement is unavailable. The sample
210 and sheath flow rates of DMA were set at 1 and 5 lpm, respectively, resulting in a measured particle
211 diameter range of 9–500 nm, with a running time of 5 min per cycle. Supersaturation in the CCNC
212 was calibrated with monodisperse ammonium sulfate particles (Rose et al., 2008) before and after the
213 campaign. The flow rates were also calibrated before and after the campaign and checked daily to
214 minimize uncertainties in droplet counting and supersaturation formed in the column (Roberts and
215 Nenes, 2005; Lance et al., 2006). SPAR deviations due to multiple-charge particles were corrected

216 using a modified algorithm based on Hagen and Alofs (1983) and Deng et al. (2011). Further details
217 regarding this system can be found in Ma et al. (2016) and Tao et al. (2021).

218 **2.2.2 H/V-TDMA measurements**

219 The mixing state of the aerosols in terms of hygroscopicity and volatility was measured using a
220 Hygroscopicity/Volatility Tandem Differential Mobility Analyzer (H/V-TDMA; Tan et al., 2013). The
221 H/V-TDMA consisted of two DMA (Model 3081 L, TSI Inc.), with the first DMA (DMA1) selecting
222 dried particles without conditioning (RH ~15%) and the second DMA (DMA2) selecting conditioned
223 particles. H/V-TDMA can operate in either H- or V-mode, controlled by a three-way solenoid valve.
224 A Nafion humidifier was used in the H-mode to condition the selected dry particles to 90% RH
225 equilibrium. The number-size distribution of humidified particles (D_p) was measured using DMA2 and
226 CPC (Model 3772, TSI Inc.). The RH-dependent hygroscopic growth factor (GF) at a specific diameter
227 (D_d) was calculated as follows:

$$228 \quad GF = \frac{D_p(RH)}{D_d} \quad (1)$$

229 where $D_p(RH)$ is the size of particles undergoing humidification. Four dry electrical mobility diameters
230 (50, 100, 150, and 200 nm) were measured in this mode. The instrument was regularly calibrated using
231 standard polystyrene latex spheres (PSL) and ammonium sulfate particles.

232 In V-mode, a heated tube evaporated the volatile coatings from the previously selected dry
233 particles. Six temperature settings were used for the heated tube, ranging from 25–200°C. The number-
234 size distributions of the heated particles were measured using DMA2 and CPC. In addition to the four
235 particle sizes measured in the H-mode, three additional particle sizes (250, 300, and 350 nm) were
236 measured in the V-mode (residence time inside the heated tube to be about 1.6 s; Hong et al., 2017).
237 The temperature-dependent shrinkage factor (SF), which is the ratio of heated particle size to dry
238 particle size without heating (D_d), is defined as:

$$239 \quad SF = \frac{D_p(T)}{D_d} \quad (2)$$

240 where $D_p(T)$ denotes the particle diameter during heating. A complete cycle of H-mode
241 measurements under one RH condition and V-mode measurements at six temperatures took
242 approximately 3 h. The Probability Density Function (PDF) of the GF (or SF) was calculated from the

243 measured density function using the inversion algorithm described by Stolzenburg and McMurry
244 (2008).

245 **2.2.3 DMA-SP2 measurements**

246 The size-resolved BC mixing states were measured using an SP2 (Droplet Measurement
247 Technology, Inc., USA) after DMA (Model 3081, TSI, USA). The DMA selected aerosols of various
248 dry particle sizes, which were then introduced into SP2. The DMA-SP2 setup was able to measure the
249 mixing states of aerosols with diameters (detection limit of approximately 80 nm based on the
250 calibration) of 100, 120, 160, 200, 235, 270, 300, 335, 370, 400, 435, 470, 500, 535, 570, 600, 635,
251 670, and 700 nm within 20 min when it was not placed after a denuder-bypass switch system (during
252 the following time periods: the 13th to the 24th of October, 09:00 am of the 5th of November to 09:00
253 am of the 8th of November). However, it only measured mixing states at diameters of 120, 160, 200,
254 250, 300, 400, and 500 nm when it was placed after a thermodenuder-bypass switch system (during
255 the following time periods: 11:00 am of the 24th of October to 08:00 am of the 5th of November, and
256 09:00 am of the 8th of November to 06:00 pm of the 17th of November). Because the HTDMA and
257 VTDMA measurements were conducted solely by a single H/VTDMA system operating in different
258 modes, the time needed for a single particle size measurement of HTDMA and VTDMA was much
259 longer than that of the DMA-SP2 system. Thus, for the same measurement cycle (2h), more particle
260 sizes were selected in the DMA-SP2 system to acquire the BC mass concentration and mixing state at
261 larger diameters than HTDMA and VTDMA.

262 The SP2 chamber had a continuous Nd:YAG laser beam with a wavelength of 1064 nm. The BC-
263 containing particles passing through the laser beam become incandescent by absorbing radiation. The
264 mass concentration of the BC was calculated by measuring the intensity of the emitted incandescent
265 light. The sheath flow/sample flow ratio was maintained at 10 for the DMA to reduce the width of the
266 diameter distribution of the selected monodisperse aerosols. Additionally, the flow rate of the SP2 was
267 changed from 0.1 to 0.12 L/min starting on the 22nd of October (allowed flow rate range of SP2: 0.03–
268 0.18 L/min from the specification). SP2 was calibrated using quadag soot particles, as reported by
269 Gysel et al. (2011). Further details regarding the calibrations are provided in Section 1 of the
270 Supplementary Information.

271 **2.3 Derivations of mixing state parameters**

272 2.3.1 Fitting SPAR curves measured by the DMA-CCNC system

273 The SPAR curves were parameterized using a sigmoidal function with three parameters. As
274 shown in Fig. S4, a sigmoidal curve generally characterized the measured SPAR. This
275 parameterization assumes that the aerosol is an external mixture of CCN-active hydrophilic and CCN-
276 inactive hydrophobic particles (Rose et al., 2010). The formula used to parameterize the SPAR ($R_a(D_d)$)
277 for a specific SS is as follows (Rose et al., 2008):

$$278 R_a(D_d) = \frac{MAF}{2} \left(1 + \operatorname{erf} \left(\frac{D_d - D_a}{\sqrt{2}\pi\sigma} \right) \right) \quad (7)$$

279 where erf denotes the error function. The Maximum Activation Fraction (MAF) is an asymptote of the
280 measured SPAR curve for large particles, as shown in Fig. S4, representing the number fraction of
281 CCNs relative to the total number of particles. D_a is the midpoint activation diameter, is linked to the
282 hygroscopicity of the CCNs, and indicates the diameter where the SPAR equals half of the MAF value.
283 The σ is the standard deviation of the cumulative Gaussian distribution function and characterizes the
284 heterogeneity of CCN hygroscopicity. In Fig. S4, the σ indicates the slope of the steep increase in the
285 SPAR curves when the diameter is close to D_a . Generally, hydrophilic particles larger than D_a can
286 become CCN. Therefore, these three parameters can be used to characterize the hygroscopicity of these
287 hydrophilic particles. This study did not consider the impact of nearly hydrophobic particles on SPAR,
288 as deviations from this parameterization scheme due to this impact were negligible at low SSs, as
289 stated in Tao et al. (2020).

290

291 2.3.2 Classification of particle type based on hygroscopicity or volatility

292 In this study, ambient aerosol particles were classified into two groups based on their
293 hygroscopicity (hydrophobic and hydrophilic) and two groups based on their volatility (non-volatile
294 and volatile) based on the measurements from H/V-TDMA (Wehner et al., 2009; Liu et al., 2011;
295 Zhang et al., 2016). Each group can be defined using the critical values of GF or SF as follows:
296 hydrophobic population: $GF < GF_C$; hydrophilic population: $GF \geq GF_C$; non-volatile population: $SF \geq SF_C$;
297 and volatile population: $SF < SF_C$.

298 The critical values of GF (GF_C) and SF (SF_C) in H/V-TDMA depend on the particle size and
299 working conditions, such as relative humidity and heating temperature. During this campaign, the SF_C

300 was set to 0.85 for all seven measured particle sizes at a temperature of 200 °C. The GF_C for the four
 301 measured particle sizes of 50, 100, 150, and 200 nm were 1.1, 1.15, 1.175, and 1.2, respectively, and
 302 the corresponding hygroscopicity parameter, κ , was approximately 0.07. These values of GF_C and SF_C
 303 divide the probability density functions (PDFs) of SF and GF into two modes as shown in Figure 2c,
 304 consistent with prior NCP studies (Liu et al., 2011; Zhang et al., 2016), and may be different from
 305 those GF_C and SF_C in other studies because of the difference in aerosol micro-physical properties. The
 306 NF for the hydrophilic group (NF_H) and volatile group (NF_V) can be calculated as follows:

$$307 \quad NF_H = \int_{GF_C}^{\infty} GF PDF(GF) dGF \quad (7)$$

$$308 \quad NF_V = \int_0^{SF_C} SF PDF(SF) dSF \quad (8)$$

309 where $GF PDF$ and $SF PDF$ are the PDFs of GF and SF, respectively, derived from H/V-TDMA
 310 measurements.

311 **2.3.3 Classification of particle type based on DMA-SP2 measurements**

312 BC-containing particles can be categorized into two groups based on coating thickness: bare
 313 BC/thinly coated BC particles and thickly coated BC particles. For the measurement of coated BC
 314 particles at SP2, the incandescence signal is generally detected later than the scattering signals and the
 315 time difference between the occurrence of the peaks of the incandescence and scattering signals is
 316 defined as the lag time (Moteki & Kondo, 2007; Sedlacek et al., 2012; Subramanian et al., 2010). The
 317 coating thickness of BC-containing particles in the SP2 measurement can be indicated by the lag time
 318 (Moteki and Kondo, 2007; Schwarz et al., 2006; Sedlacek et al., 2012; Subramanian et al., 2010;
 319 Metcalf et al., 2012), which has exhibited a clear two-mode distribution in previous studies (Zhang et
 320 al., 2018; Zhao et al., 2021). A critical lag time threshold can be used to differentiate between the
 321 different types of BC-containing particles and calculate the NF of bare and coated BC particles in the
 322 total identified particles. In this study, a two-mode distribution of the lag time (Δt) was observed, and
 323 a critical value of 0.8 μs was used to classify the BC-containing particles into thinly coated (or bare)
 324 BC ($\Delta t < 0.8 \mu s$) and thickly coated BC ($\Delta t \geq 0.8 \mu s$). The definitions of all abbreviations are listed in
 325 Table 1.

326 **3 Results and discussions**

327 **3.1 Campaign overview**

328 The time series of the meteorological parameters, aerosol mixing state measurements using
329 different techniques, and mass concentrations of the aerosol chemical components are shown in Fig.
330 1. In detail, the measurements of aerosol mixing states include SPAR at an SS of 0.08% by DMA-
331 CCNC, GF-PDF (PDF of GF) at 200 nm by HTDMA, SF-PDF (PDF of SF) at 200 nm and 200 °C by
332 VTDMA, and lag time PDF of 200 nm BC-containing particles by DMA-SP2. The SIA, SOA, POA,
333 and BC mass concentrations are shown in Fig. 1 (b). Three periods with significantly different aerosol
334 pollution conditions were identified during the campaign. As shown in Fig. 1(b), before the 23rd of
335 October (moderately polluted period), the accumulation of aerosols led to SIA mass concentrations
336 $<20 \mu\text{g}/\text{m}^3$. In contrast, the highest mass concentrations of SOA, POA, and BC all reached $10 \mu\text{g}/\text{m}^3$.
337 The mass concentrations of different aerosol components increased significantly from the 23rd of
338 October to the 6th of November (heavily polluted period with an average non-refractory PM_{10} mass
339 concentration of $49.5 \pm 22.5 \mu\text{g}/\text{m}^3$) and decreased to much lower levels after the 6th of November
340 (clean period with a non-refractory PM_{10} mass concentration of $5.1 \pm 3.3 \mu\text{g}/\text{m}^3$). Two particle groups
341 were identified concerning the CCN activity, hygroscopicity, volatility, and coating thickness, as
342 demonstrated by the SPAR, GF-PDF, SF-PDF, and lag-time PDF of BC-containing particles.
343 Significant variations in the aerosol mixing states were also observed during the three periods with
344 different pollution conditions, as demonstrated by the variations in SF-PDF measured by VTDMA.
345 For example, the SF of the non-volatile particle group decreased during the heavily polluted period.
346 Aerosol mixing states may have changed because of various transformations in existing aerosol
347 particles and distinct secondary formation processes under different pollution conditions (Kuang et al.,
348 2020; Tao et al., 2021; Shi et al., 2022; Yang et al., 2022). Diurnal variations in the mass concentrations
349 of different aerosol chemical components and mixing states can be observed in the variations in the
350 SPAR measurements, as previously observed in this region (Liu et al., 2011; Ma et al., 2012; Kuang
351 et al., 2015; Tao et al., 2020).

352 Fig. 2 shows the campaign-averaged SPAR at the three SSs, PDF of the lag time of BC-containing
353 particles, GFPDF, and SFPDF at 200 °C for different particle sizes. The sigmoidal SPAR curves were
354 characterized by a rapid increase, followed by a gradual increase to unit 1, similar to the measured

355 SPAR curves previously observed in this region (Deng et al., 2011; Zhang et al., 2014; Ma et al., 2016;
356 Tao et al., 2018). At lower SSs, the particle size required for CCN activation was larger; thus, rapid
357 increases in the SPAR curves occurred at larger particle sizes as expected. In addition, the maximum
358 AR of the SPAR curves decreases as fewer particles are CCN-active under low SSs. For the three
359 measured SSs, the particle sizes where SPAR equals approximately 0.5 are approximately 90, 120,
360 and 180 nm for the three SSs of 0.08%, 0.14%, and 0.22%, respectively, consistent with the average
361 D_a (see Eq. 7) values of the campaign. The NF of CCN-active particles in large-diameter ranges (which
362 varies with SS and, for example, is greater than 200 nm for 0.08%) can be indicated by the gradual
363 increase in the SPAR curves and quantified by the fitting parameter, MAF (see Eq. 7). The PDFs of
364 the lag time, GF, and SF were all characterized by a bimodal distribution, which indicates two particle
365 groups of BC-containing particles with different coating thicknesses, hygroscopicity, and volatility.
366 The variations in the aerosol mixing states were further analyzed based on the measured mixing state
367 parameters.

368 **3.2 Intercomparisons among aerosol mixing state parameters derived using four techniques**

369 The size-dependent characteristics of the aerosol mixing state parameters derived from the
370 measurements of the four techniques and the MFs of different aerosol chemical components during
371 the three pollution periods are shown in Fig. 3. In general, the size-dependent characteristics of MAF,
372 NF_H , NF_V , and NF_{noBC} were similar, suggesting that they were likely dominated by the same particle
373 group, namely BC-free particles. This particle group had the highest number fraction (>0.7) during the
374 heavily polluted period and the lowest number fraction (down to 0.5) during the clean period, with the
375 fraction decreasing with increasing particle size. This suggests that primary emissions tend to have
376 higher number fractions of BC-containing particles in larger diameter ranges; for example, the number
377 fraction of BC-containing particles increases from ~ 0.1 to ~ 0.4 as the particle size increases from 200
378 to 500 nm during the clean period. Because the bulk aerosol MF is mostly contributed by particles >300
379 nm, there may have been more hydrophilic, volatile, CCN-active, and BC-free particles with larger
380 sizes (>300 nm) during the heavily polluted period owing to strong SA formation in larger diameter
381 ranges (Kuang et al., 2020), resulting in a higher NF of these particles compared to the clean period.
382 As for R_{exBC} , which is defined as the number concentration ratio of externally mixed BC particles in
383 total BC-containing particles, the small size dependence of R_{exBC} during the moderately polluted period

384 might have been associated with stronger primary emissions, while the decrease in R_{exBC} with
385 increasing particle diameter in the polluted period confirmed that SA formation is more efficient for
386 particles with larger diameters.

387 As for the difference among the aerosol mixing state parameters, NF_V and NF_{noBC} agreed with
388 each other with a <0.1 difference, and both were higher than NF_H by at least $0.1 NF_H$ in the moderately
389 polluted period. Compared with NF_{noBC} , NF_V was higher during the heavily polluted period, when the
390 nitrate mass fraction was the highest ($\sim 30\%$). The SOA mass fraction was the lowest ($\sim 7\%$) among all
391 three periods, suggesting that some BC-containing particles in this period were also identified as
392 volatile, consistent with the fact that the formation of semi-volatile nitrate in BC-containing particles
393 increases their volatility. However, during the clean period, NF_V was even lower than NF_{noBC} ,
394 suggesting that some BC-free particles were characterized as low volatile and non-negligible number
395 fractions of BC-free particles dominated these less volatile aerosol components, which were likely less
396 volatile organic aerosols (not likely contributed by BC-containing particles with a BC smaller than the
397 SP2 detection limit, because this type of volatile BC-containing particles has an SF lower than 0.4
398 ($=80 \text{ nm}/200 \text{ nm}$), which is substantially lower than the threshold SF of 0.85 for NF_V calculation). In
399 addition, the MAF values generally agreed with the NF_H during the clean period. However, they were
400 larger than the NF_H during the moderately and heavily polluted periods (by ~ 0.2) when the POA/SOA
401 mass fractions were higher ($\sim 40\%$ vs. $\sim 35\%$). POA generally has a lower hygroscopicity than SOA.
402 The critical κ of hydrophilic mode aerosols was 0.07, suggesting that a higher number fraction of
403 aerosols had κ below 0.07 (i.e., hydrophobic mode aerosols in this study) during the moderately
404 polluted period. However, under supersaturated conditions, they demonstrate enhanced hygroscopicity
405 by becoming CCN-active. NF_H was consistently lower than NF_V and NF_{noBC} (the average difference
406 between NF_H and NF_{noBC} was approximately 0.2). As mentioned above, NF_H was also lower than MAF
407 during moderately polluted periods, and there may be a significant number fraction of volatile BC-free
408 particles with hygroscopicity lower than the critical κ value of 0.07; however, they were still CCN-
409 active and therefore not fully hydrophobic.

410 The diurnal variations in MAF, NF_H , NF_V , and NF_{noBC} , along with the MFs of the aerosol
411 chemical components during the three periods, are shown in Fig. 4. Except for a particle size of 50 nm,
412 the diurnal variations in these four mixing state parameters were generally similar for all measured

413 sizes. The different diurnal variations at a particle size of 50 nm may be due to the different effects of
414 emissions and aging processes on the different aerosol modes, as particles <100 nm mainly reside in
415 the Aitken mode, which is where particles >100 nm mainly reside in the accumulation mode (Wang et
416 al., 2022). For particles >100 nm (Fig. 4 and S5), there was a maximum in the afternoon for MAF,
417 NF_H , NF_V , and NF_{noBC} , indicating a peak during this time due to an increase in SA compositions, such
418 as nitrate and SOA, and a decrease in POA and BC. Diurnal variations in the aerosol mixing state
419 parameters and chemical compositions were more pronounced during the moderately polluted period.
420 During heavily polluted periods, the diurnal variation was least pronounced for NF_V and most
421 pronounced for NF_H . In the clean-air period, there was another maximum at midnight for MAF and
422 NF_{noBC} , which may be attributed to the diurnal variations in SA compositions, such as sulfate and SOA,
423 and the decrease in BC and FFOA. The average-size dependence of the aerosol mixing state parameters
424 over different time ranges during a heavily polluted period is shown in Fig. S6. It can be seen that the
425 differences among the four parameters were the least from 12:00 to 18:00, with the most SOA and the
426 least POA. This is consistent with the results shown in Fig. 3, where the difference between the MAF
427 and NF_H decreased when the POA mass fractions were the smallest. R_{exBC} tended to be lower during
428 the daytime, and its diurnal variation was more significant for larger particle sizes. In general, the
429 diurnal variations for R_{exBC} were opposite to those of NF_{noBC} and agreed better with those of the
430 primary aerosol MFs. This is because BC particles originate from primary emissions and are mainly
431 mixed externally. After aging in the atmosphere, BC particles can be coated by SAs, resulting in more
432 coated BC particles and fewer externally mixed BC particles. As SAs tend to form on larger particles,
433 the diurnal variations in SA formation may significantly affect the R_{exBC} of larger particle sizes.

434 As summarized in Table. S1, the comparison among MAF, NF_H , NF_V , and NF_{noBC} was
435 conducted based on their correlations with different particle sizes. Note that the MAF at SSs of 0.08%,
436 0.14%, and 0.22% were used for comparison at 200, 150, and 100 nm particle sizes. This is because
437 the diameter range of rapid increases in the SPAR curves is determined by aerosol hygroscopicity in
438 this particle size range. The midpoints of the rapidly increasing diameter ranges of the SPAR curves
439 at SSs of 0.08%, 0.14%, and 0.22% were approximately 180 nm, 120 nm, and 90 nm, respectively (as
440 shown in Fig. 2). In general, there were moderate correlations ($r \sim -0.5$) between MAF, NF_H , and NF_V ,
441 suggesting that a similar particle group contributed to the dominance of CCN-active, hygroscopic, and

442 volatile aerosols (Zhang et al., 2016). The agreement between MAF and N_{F_V} was slightly higher than
443 that between MAF and N_{F_H} or between N_{F_H} and N_{F_V} . In detail, compared to the other two, the
444 agreement between MAF and N_{F_V} has a similar correlation coefficient ($r \sim 0.65$) and a smaller
445 systematic difference (slope and intercept were much closer to 1 and 0, respectively). This is consistent
446 with the previous finding that a substantial number fraction of volatile but less hygroscopic aerosols
447 are CCN-active. For smaller particle sizes, the correlation became weaker ($r \sim 0.4$), whereas the degree
448 of reduction was the lowest for the correlation between MAF and N_{F_V} ($r \sim 0.529$).

449 3.3 Impacts of primary aerosol emissions on aerosol mixing states and parameter 450 intercomparisons

451 Fig. 5 presents the correlation between each aerosol mixing state parameter at 200 nm and the
452 MF of each primary organic aerosol composition during the three periods. The four mixing state
453 parameters (MAF, N_{F_H} , N_{F_V} , and $N_{F_{noBC}}$) were negatively correlated with MF_{FFOA} and MF_{BBOA} .
454 However, the anticorrelation with MF_{FFOA} (-0.45~-0.74) was much stronger than MF_{BBOA} (-0.10~-
455 0.45). Biomass-burning emissions and fossil fuel emissions are the two major sources of BC in the
456 NCP (Yang et al., 2022), and $N_{F_{noBC}}$ was negatively correlated with MF_{FFOA} ($r = -0.49$) and weakly
457 correlated ($r = -0.18$) with MF_{BBOA} , suggesting that fossil fuel emissions were likely the dominant
458 source of BC during this field campaign. The negative correlation between MAF and MF_{FFOA} was
459 weaker than that of $N_{F_{noBC}}$ with MF_{FFOA} (-0.62 vs. -0.49). In particular, at the same MF_{FFOA} , the MAF
460 was lower than $N_{F_{noBC}}$, demonstrating that some BC-free particles were CCN-inactive and were likely
461 mainly composed of organic aerosols from fossil fuel combustion emissions. The negative correlation
462 between N_{F_V} and MF_{FFOA} was slightly weaker than between $N_{F_{noBC}}$ and MF_{FFOA} (-0.56 vs. -0.49). At
463 the same MF_{FFOA} , $N_{F_{noBC}}$ was close to N_{F_V} , and considering that BC-containing particles were
464 dominated by thinly coated BC most of the time (Fig. 5), this demonstrates that the non-volatile
465 population identified by V-TDMA was mainly contributed by BC-containing particles. N_{F_H} had the
466 lowest negative correlation with MF_{FFOA} ($r = -0.74$), demonstrating significant contributions from fossil
467 fuel emissions to nearly hydrophobic aerosol populations. At the same MF_{FFOA} , for example, when
468 conditions of $MF_{FFOA} > 0.1$ were met, N_{F_H} (<0.7) demonstrated a noticeable decrease compared to
469 $N_{F_{noBC}}$ (>0.7), and N_{F_H} showed a negative correlation with both MF_{BBOA} and MF_{FFOA} , suggesting that
470 a substantial portion of nearly hydrophobic particles originated from FFOA- or BBOA-dominant rather

471 than BC-containing particles. Additionally, markedly different correlations were observed between
472 MAF and MF_{FFOA} ($r=-0.62$), and between MAF and MF_{BBOA} ($r=-0.2$), implying that nearly
473 hydrophobic but CCN-active aerosols likely originated from biomass burning. The correlations
474 between the ratio of thinly coated BC in the total BC-containing particles (R_{exBC}) and the MFs of
475 BBOA and FFOA are shown in Fig. 6. Weak correlations ($r<0.3$) between R_{exBC} and MF_{BBOA} and
476 MF_{FFOA} were observed. However, R_{exBC} tended to increase with MF_{FFOA} , suggesting that BC-
477 containing particles emitted from fossil fuel combustion tended to be more externally mixed with other
478 aerosol components than those emitted from biomass burning, which is consistent with the results of
479 previous studies (Schwarz et al., 2008; Laborde et al., 2013; Liu et al., 2017; Zhang et al., 2020). These
480 results demonstrate remarkably different mixing states and the physical and chemical properties of
481 fossil fuel combustion and biomass-burning aerosols.

482 The impact of primary emissions on the differences among the four aerosol mixing state
483 parameters at a particle size of 200 nm was analyzed and is shown in Fig. 7. The difference between
484 NF_{noBC} and NF_H ($NF_{noBC}-NF_H$) was significantly positively correlated with MF_{FFOA} and MF_{BBOA}
485 ($r>0.5$), suggesting that a substantial proportion of POA resided in BC-free particles and was volatile,
486 but contributed substantially to nearly hydrophobic aerosols; as did the differences between NF_V and
487 NF_H (NF_V-NF_H). The MFs of BBOA and FFOA were poorly correlated with the differences between
488 the MAF and NF_V ($MAF-NF_V$), MAF and NF_{noBC} ($MAF-NF_{noBC}$), and NF_V and NF_{noBC} (NF_V-NF_{noBC})
489 (Fig. S7). The difference between MAF and NF_H was positively correlated with MF_{BBOA} , further
490 suggesting that BBOA contributed to nearly hydrophobic aerosols under subsaturated conditions;
491 however, their hygroscopicity was enhanced, and they became CCN-active under supersaturated
492 conditions. The enhanced hygroscopicity of BBOA under supersaturated conditions may be attributed
493 to: (1) surface tension lowered by surface-active organic solutes (Hodas et al., 2016; Ruehl et al., 2016);
494 (2) liquid–liquid phase separation (Ovadnevaite et al., 2017; Liu et al., 2018); (3) dissolution of
495 sparingly soluble compounds at higher saturated conditions (Wex et al., 2009; Dusek et al., 2011); (4)
496 highly viscous organic aerosol which takes up water by surface water adsorption under sub-saturated
497 conditions and by absorption of water under super-saturated conditions (Pajunoja et al., 2015). The
498 correlations between the mixing-state parameters and primary aerosol composition during the
499 campaign and different pollution periods are summarized in Fig. S7.

500 In general, both field and laboratory studies have shown that primary organic aerosols from the
501 combustion of biomass and fossil fuels are less hygroscopic. In laboratory experiment, it is found
502 that organic aerosols produced by fossil fuels have very low hygroscopicity, significantly less than
503 0.1 (Vu et al., 2015, 2017; Fofie et al., 2018; Zhang et al., 2018; Mukherjee et al., 2021).
504 Observations have also found that the organic aerosols associated with fossil fuel combustion have
505 low hygroscopicity, which may be due to the poorly water soluble substances in FFOA (Qiu et al.,
506 2019; Li et al., 2021). The aerosol composition produced by biomass burning is complex, with a
507 large number of organic aerosols (BBOA) and inorganic components being produced at the initial
508 stage, making important contributions to CCN (Spracklen et al., 2011; Bougiatioti et al., 2016;
509 Pöhlker et al., 2018). These primary organic aerosols (i.e. BBOA) is generally semi-volatile (May et
510 al. 2013) and less hygroscopic (Engelhart et al., 2012; Hennigan et al., 2012), which has a negative
511 contribution to overall hygroscopicity (Bougiatioti et al., 2016; Kuang et al., 2020b, 2021, Cai et al.,
512 2022), resulting in weaker overall aerosol hygroscopicity in the initial stage of the biomass burning
513 (Engelhart et al., 2012, Hennigan et al., 2012, Pöhlker et al., 2018). However, laboratory experiments
514 found that BBOA may contain organic substances with different hygroscopicity under different
515 saturation ratios (Malek et al., 2022), lead to increased hygroscopicity and enhanced CCN activity of
516 BBOA under supersaturation conditions (Hersey et al., 2013). Our results generally agree with
517 previous studies and provide evidences of the enhanced CCN activity of BBOA under
518 supersaturation conditions in field campaigns. Furthermore, the different impacts of aerosols emitted
519 from biomass burning and fossil fuel combustion on CCN is directly observed in this campaign used
520 newly developed advanced aerosol-cloud sampling system, which show that biomass burning
521 aerosols are efficient CCN even under low supersaturations ($<0.05\%$), however, aerosols from fossil
522 fuel combustions can only activate at higher supersaturations ($\sim >0.14\%$). These results suggest
523 simultaneous measurements of aerosol GF distributions, SPAR curves and BC mixing states and
524 their comparisons could shed novel insights into different synergistic hygroscopic, volatile and
525 activation properties of aerosols from different sources in the atmosphere.

526 **3.4 Impacts of SA formation on aerosol mixing states and parameter intercomparisons**

527 The correlations between the aerosol mixing state parameters at 200 nm and the MF of each SA
528 component are presented in Fig. 8 for three periods, and the entire campaign is presented. The analysis

529 is conducted at only 200 nm, where all four aerosol mixing state parameters were measured to compare
530 the four aerosol mixing state parameters and their relationships with aerosol chemical components
531 simultaneously. Generally, MAF, NF_H , NF_V , and NF_{noBC} exhibited strong positive correlations with
532 MF_{NH_4} ($r > 0.5$). This is likely because ammonium was mainly formed through neutralizing sulfuric and
533 nitric acids with ammonia; therefore, variations in ammonium better represent overall secondary
534 inorganic aerosol formation. As shown in Fig. 3, the secondary inorganic aerosol components
535 dominated SA (the mass ratio between SIA and SA is approximately 70%), indicating that SA
536 formation was primarily composed of secondary inorganic aerosol formation, which explains the
537 weaker correlation with SOA ($r \sim 0.3$), as shown in Fig. 8.

538 During the clean-air period, when the MFs of SOA and sulfate were both above 15%, all four
539 parameters had a strong positive correlation with MF_{SO_4} and MF_{SOA} ($r > 0.5$), suggesting that when a
540 clean background air mass with higher mass fractions of sulfate and SOA prevailed, the local primary
541 emissions that contributed substantially to BC-containing and less hygroscopic POA aerosols became
542 less significant. The positive correlations between the MAF and SA components have been extensively
543 discussed by Tao et al. (2021), who found that SA formation enhances the hygroscopicity of nearly
544 hydrophobic aerosols, thereby increasing CCN activity. This also explains the strong correlation
545 between the NF_H or MAF and ammonium formation. The strong positive correlations between NF_V
546 and SA formation ($r \sim 0.6$) are consistent with the fact that nitrate dominates SA formation during this
547 campaign and is semi-volatile. For the first time, strong positive correlations between NF_{noBC} and SA
548 formation were observed ($r = 0.6$). NF_{noBC} depends primarily on the relative variation between BC-
549 containing and BC-free particles. The increase in NF_{noBC} at 200 nm as a function of the SA MF
550 suggests that SAs migrated higher mass fraction of BC-free particles with particle size smaller than
551 200 nm to particle size of 200 nm, suggesting that SAs tended to form more quickly on BC-free
552 particles than on BC-containing particles with BC higher than SP2 detection limit. Recent studies
553 reported that catalyst or photochemical reactions on BC particles can contribute the formation of
554 secondary aerosols (Zhang et al., 2020; Zhang et al., 2021). Our results may indicate SA formation on
555 BC particles might not be a significant pathway that contributes substantially to haze formation, and
556 the underlying mechanisms need to be further resolved.

557 The effects of SA formation on the differences between the four aerosol mixing state parameters
558 were studied and are illustrated in Fig. 9. The two OOA factors (OOA1 and OOA2) were formed
559 through different chemical pathways. The difference between NF_{noBC} and NF_H ($NF_{noBC}-NF_H$) showed
560 a strong negative correlation with MF_{NH_4} and MF_{NO_3} (mainly -0.6), as did the differences between NF_V
561 and NF_H (NF_V-NF_H). Ammonium nitrate is a pure-scattering semi-volatile component with strong
562 hygroscopicity, the increase of its mass fraction can enhance both aerosol volatility and hygroscopicity,
563 therefore resulting in a smaller difference between NF_{noBC} , NF_H , and NF_V .

564 Furthermore, the difference between NF_V and NF_H showed a positive correlation with MF_{OOA2}
565 and a negative correlation with MF_{OOA1} , indicating different volatility and hygroscopicity of the two
566 SOA factors. The differences between NF_V and NF_H concerning the MF of OOA1 and OOA2 are
567 shown in Fig. 9(e) and (f), respectively. As previously noted, NF_V was generally higher than NF_H , and
568 the difference between the two decreased with increasing MF_{OOA1} , which was generally smaller than
569 0.3. This suggests that the formation of OOA1 enhances the hygroscopicity of volatile particles, which
570 aligns with the highest oxidation state of OOA1 (higher O/C but lower H/C compared to OOA2) and
571 has a significant and overall positive impact on aerosol hygroscopicity (Cerully et al., 2015; Thalman
572 et al., 2017; Zhang et al., 2023). A positive correlation was observed between NF_V and MF_{OOA2}
573 ($r \sim 0.25$).

574 In contrast, the correlation between NF_H and MF_{OOA2} was weak (R was close to 0), implying that
575 OOA2 might be semi-volatile but only weakly hygroscopic, which could contribute to NF_V being
576 higher than NF_H as OOA1 increases. The difference between NF_{noBC} and NF_V ($NF_{noBC}-NF_V$) was
577 negatively correlated with MF_{NO_3} , which is consistent with the semi-volatile nature of nitrate. The
578 negative correlation between $NF_{noBC}-NF_V$ and MF_{OOA2} indicates that the difference is smaller when
579 there is more OOA2, implying that OOA2 is also a semi-volatile compound and is likely formed
580 mainly on BC-free particles (particles with BC mass lower than detection limit are not excluded). The
581 correlations between the differences between NF_V-MAF and $NF_{noBC}-MAF$ and the MF of each SA
582 composition were very weak. The impacts of SA formation on BC mixing states are shown in Fig. S8.
583 In general, the NF of thinly coated BC has a negative correlation with SIA and a weak association with
584 SOA, suggesting that SIA formation mainly enhances the thickness of the BC coating. The correlations
585 between the mixing state parameters and SA composition during the campaign and different pollution

586 periods are summarized in Fig. S9. Our results on OOA agree with previous studies, that OOA are
587 reported to be volatile (Kim et al., 2020; Cai et al., 2022) but can have a positive or negative impact
588 on hygroscopicity depending on its oxidation level (Kim et al., 2020; Kuang et al., 2021; Cai et al.,
589 2022).

590 In addition to changes in the MFs of SA compositions, the accumulation of SA pollution may
591 provide insights into the impact of SA formation on aerosol mixing states. As shown in Fig. 10(a),
592 during the heavily polluted periods, there were two distinct pollution accumulation processes from the
593 23rd to the 27th of October and from the 28th to the 31st of October, respectively. During the pollution
594 accumulation process, the mass concentration of SAs increased by approximately three-fold, indicating
595 the rapid formation of secondary compositions and a significant increase in NR-PM₁ mass
596 concentration. Fig. 10(b) and (c) illustrate that this increase in SAs significantly enlarged the value of
597 aerosol mixing state parameters, including MAF, NF_V, NF_H, and NF_{noBC}, which increased from
598 approximately 0.5 to 0.8 with evident diurnal variations. This highlights the impact of SA formation
599 on the aerosol mixing states and the importance of studying the pollution accumulation processes of
600 SAs. The enhancements in the different aerosol mixing state parameters during the pollution
601 accumulation process were not uniform. MAF and NF_H initially exhibited lower values than NF_V and
602 NF_{noBC}; however, their later enhancement was stronger than that of NF_{noBC}. Fig. 10(d) and (e) show
603 the difference between NF_{noBC} and NF_V at 200 and 300 nm as a function of SA mass concentrations
604 during these two pollution periods, which clearly shows how, during SA formation, NF_V became
605 higher than NF_{noBC} while NF_V remained close to the NF of thickly coated BC-containing particles
606 (NF_{CBC}) plus NF_{noBC} (NF_{CBC}+NF_{CBC}). These results suggest that SA formation increases the volatility
607 of BC-free and BC-containing particles, leading to an increased NF_V compared with NF_{noBC}. Almost
608 all BC-free particles and some BC-containing particles become volatile during the accumulation of
609 pollution.

610

611 **4. Conclusions**

612 The aerosol mixing state is one of the most important physicochemical properties of aerosol
613 particles and significantly affects their optical properties and the CCN activity of aerosol particles. The
614 aerosol mixing states vary significantly with complex aerosol emissions and atmospheric

615 transformations. In this study, aerosol mixing states derived from CCN activity, hygroscopicity,
616 volatility, and BC particle observations, along with their relationship to primary aerosol emissions and
617 SA formation, were systematically analyzed based on simultaneous measurements of CCNC,
618 H/VTDMA, and SP2. Statistical analysis demonstrated that the NFs of CCN-active, hygroscopic, and
619 volatile particles were generally positively correlated and mainly contributed by BC-free particles.
620 Therefore, four mixing state parameters were all negatively correlated to either the MFs of BBOA or
621 FFOA because fossil fuel combustion and biomass burning were the two major sources of BC-
622 containing particles during this field campaign. However, the differences between these mixing state
623 parameters varied significantly under different conditions, have shed new insights into aerosol physical
624 and chemical properties and even secondary aerosol formation mechanisms.

625 Fossil fuel combustion and biomass burning emissions represent two major primary sources of
626 global aerosol burden and are dominant primary aerosol sources in this campaign. It is known that the
627 chemical compositions of both these primary sources are dominated by organics and BC. However,
628 the intercomparison results among instruments revealed significant differences in the physical and
629 chemical properties of aerosols emitted from these two sources. The combination of HTDMA, DMA-
630 SP2, as well as aerosol source apportionment confirmed that substantial portions of BC-free aerosols
631 from both biomass burning and fossil fuel combustion are nearly hydrophobic under sub-saturated
632 conditions. Additionally, BC from fossil fuel combustion tends to be more externally mixed with other
633 aerosol compositions than those from biomass burning. However, additional insights from DMA-CCN
634 measurements revealed that substantial portions of BC-free aerosols, nearly hydrophobic from biomass
635 burning, could serve as CCN, while a substantial portion of those from fossil fuel combustion could
636 not. Previous studies have confirmed the hygroscopicity difference of aerosols from biomass burning
637 under sub- and supersaturated conditions in laboratory settings; however, such differences have rarely
638 been confirmed in field measurements. Moreover, comparisons between sub- and supersaturated
639 conditions for aerosols from fossil fuel combustion have been rarely undertaken, even in laboratory
640 studies. This finding is quite important because the ability of primary organic aerosols from biomass
641 burning and fossil fuel combustion is often treated as the same in models (Liu et al., 2021; Pöhlker et
642 al., 2023).

643 Secondary aerosol formation substantially alters aerosol mixing state. The different variations in
644 mixing state parameters can also help reveal mechanisms of secondary aerosol formation. For example,
645 the two resolved SOA factors exhibited different impacts on the differences between N_{F_V} and N_{F_H}
646 ($N_{F_V}-N_{F_H}$), and their correlations with N_{F_V} and N_{F_H} revealed that OOA_1 was more hygroscopic but
647 less volatile, suggesting distinct formation mechanisms for these two OOA factors. Further analysis
648 might help link SOA formation mechanisms to aerosol physical properties, which is important for
649 connecting aerosol chemistry to aerosol climate effects determined by aerosol physicochemical
650 properties. Additionally, variations in size-resolved $N_{F_{noBC}}$ revealed that secondary organic and
651 inorganic aerosol formations led to the migration of BC-free particles towards larger diameters more
652 quickly than that of BC-containing particles. This phenomenon is more likely to occur when aqueous
653 pathways dominate secondary aerosol formation because BC-containing particles generally exhibit
654 weak hygroscopicity and do not favor aqueous processes.

655 The findings of this study highlight the markedly different effects of primary emissions and SA
656 formation on aerosol mixing states and suggest that comparisons of aerosol mixing states obtained
657 using various techniques are useful for gaining insights into the hygroscopicity, volatility, and CCN
658 activity of different aerosols. Recommendations are listed for future studies based on the findings of
659 this study: (1) When exploring the impact of aerosol emissions and secondary aerosol formations on
660 aerosol hygroscopic under sub- and supersaturated conditions, we recommend employing
661 simultaneous DMA-SP2 measurements to better represent BC characteristics; (2) Simultaneous DMA-
662 CCNC, V-HTDMA, and DMA-SP2 measurements could enhance studies on secondary aerosol
663 formation mechanisms. Conversely, if formation mechanisms and pathways are clear, these
664 measurements could elucidate how secondary aerosol formation impacts aerosol physical properties
665 from different aspects. (3) To be cautious in the application of aerosol mixing state parameters from
666 HV-TDMA to conduct aerosol optical property investigations because the suitability of HV-TDMA-
667 derived mixing state parameters for representing BC mixing states is largely dependent on the
668 composition and mass of the secondary aerosols, and DMA-SP2 measurements are recommended for
669 this purpose.

670

671 **Data availability.** The data used in this study are available from the corresponding author upon request
672 Ye Kuang (kuangye@jnu.edu.cn) and Li Liu (liul@gd121.cn)

673 **Competing interests.** The authors declare that they have no conflict of interest.

674

675 **Author Contributions.**

676 YK and WY planned this campaign and YK designed the aerosol experiments and conceived this
677 research together with JC, and JC wrote the manuscript. JC performed measurements of CCNC, BL
678 performed measurements of SP2 and analyzed SP2 datasets with the help of GZ, WQ and YL
679 performed AMS measurements, LL performed HV-TDMA measurements and conducted post-data
680 processing as well as some of data analysis. BX, HX, MMZ, HZ and SR participated this campaign
681 and helped instruments maintenance. GZ provided full support for the campaign. All authors
682 contributed to discussions and revisions of this paper.

683 **Financial supports.** This work is supported by National Natural Science Foundation of China
684 (42175083, 42175127, 42275066), the Guangzhou Science and Information Technology Bureau
685 Project (2023A04J0941), the Guangdong Provincial Key Research and Development Program (grant
686 no. 2020B1111360003), the Science and Technology Innovation Team Plan of Guangdong
687 Meteorological Bureau (grant no. GRMCTD202003).

688

689 **References**

690 Adachi, K., Sedlacek, A. J., Kleinman, L., Chand, D., Hubbe, J. M., and Buseck, P. R.: Volume
691 changes upon heating of aerosol particles from biomass burning using transmission electron
692 microscopy, *Aerosol Science and Technology*, 52, 46–56,
693 <https://doi.org/10.1080/02786826.2017.1373181>, 2018.

694 Adachi, K., Sedlacek, A. J., Kleinman, L., Springston, S. R., Wang, J., Chand, D., Hubbe, J. M.,
695 Shilling, J. E., Onasch, T. B., Kinase, T., Sakata, K., Takahashi, Y., and Buseck, P. R.: Spherical tarball
696 particles form through rapid chemical and physical changes of organic matter in biomass-burning
697 smoke, *Proceedings of the National Academy of Sciences*, 116, 19336–19341,
698 <https://doi.org/10.1073/pnas.1900129116>, 2019.

699 Bond, T. C., Doherty, S. J., Fahey, D. W., Forster, P. M., Berntsen, T., DeAngelo, B. J., Flanner,
700 M. G., Ghan, S., Kaercher, B., Koch, D., Kinne, S., Kondo, Y., Quinn, P. K., Sarofim, M. C., Schultz,
701 M. G., Schulz, M., Venkataraman, C., Zhang, H., Zhang, S., Bellouin, N., Guttikunda, S. K., Hopke,
702 P. K., Jacobson, M. Z., Kaiser, J. W., Klimont, Z., Lohmann, U., Schwarz, J. P., Shindell, D.,
703 Storelvmo, T., Warren, S. G., and Zender, C. S.: Bounding the role of black carbon in the climate
704 system: A scientific assessment, *Journal of Geophysical Research-Atmospheres*, 118, 5380–5552,
705 <https://doi.org/10.1002/jgrd.50171>, 2013.

706 Bougiatioti, A., Bezantakos, S., Stavroulas, I., Kalivitis, N., Kokkalis, P., Biskos, G.,
707 Mihalopoulos, N., Papayannis, A., and Nenes, A.: Biomass-burning impact on CCN number,
708 hygroscopicity and cloud formation during summertime in the eastern Mediterranean, *Atmos. Chem.*
709 *Phys.*, 16, 7389–7409, <https://doi.org/10.5194/acp-16-7389-2016>, 2016.

710 Cai, M., Tan, H., Chan, C. K., Mochida, M., Hatakeyama, S., Kondo, Y., Schurman, M. I., Xu,
711 H., Li, F., Shimada, K., Li, L., Deng, Y., Yai, H., Matsuki, A., Qin, Y., and Zhao, J.: Comparison of
712 Aerosol Hygroscopicity, Volatility, and Chemical Composition between a Suburban Site in the Pearl
713 River Delta Region and a Marine Site in Okinawa, *Aerosol and Air Quality Research*, 17, 3194–3208,
714 <https://doi.org/10.4209/aaqr.2017.01.0020>, 2017.

715 Cai, M., Huang, S., Liang, B., Sun, Q., Liu, L., Yuan, B., Shao, M., Hu, W., Chen, W., Song, Q.,
716 Li, W., Peng, Y., Wang, Z., Chen, D., Tan, H., Xu, H., Li, F., Deng, X., Deng, T., Sun, J., and Zhao,
717 J.: Measurement report: Distinct size dependence and diurnal variation in organic aerosol
718 hygroscopicity, volatility, and cloud condensation nuclei activity at a rural site in the Pearl River Delta
719 (PRD) region, China, *Atmos. Chem. Phys.*, 22, 8117–8136, <https://doi.org/10.5194/acp-22-8117-2022>,
720 2022.

721 Canagaratna, M. R., Jimenez, J. L., Kroll, J. H., Chen, Q., Kessler, S. H., Massoli, P., Hildebrandt
722 Ruiz, L., Fortner, E., Williams, L. R., Wilson, K. R., Surratt, J. D., Donahue, N. M., Jayne, J. T., and
723 Worsnop, D. R.: Elemental ratio measurements of organic compounds using aerosol mass
724 spectrometry: characterization, improved calibration, and implications, *Atmos. Chem. Phys.*, 15, 253–
725 272, <https://doi.org/10.5194/acp-15-253-2015>, 2015.

726 Cerully, K. M., Bougiatioti, A., Hite Jr., J. R., Guo, H., Xu, L., Ng, N. L., Weber, R., and Nenes,
727 A.: On the link between hygroscopicity, volatility, and oxidation state of ambient and water-soluble
728 aerosols in the southeastern United States, *Atmos. Chem. Phys.*, 15, 8679–8694,
729 <https://doi.org/10.5194/acp-15-8679-2015>, 2015.

730 Chen, C., Qiu, Y., Xu, W., He, Y., Li, Z., Sun, J., Ma, N., Xu, W., Pan, X., Fu, P., Wang, Z., and
731 Sun, Y.: Primary Emissions and Secondary Aerosol Processing During Wintertime in Rural Area of
732 North China Plain, *Journal of Geophysical Research: Atmospheres*, 127, e2021JD035430,
733 <https://doi.org/10.1029/2021JD035430>, 2022.

734 Chen, J., Budisulistiorini, S. H., Miyakawa, T., Komazaki, Y., and Kuwata, M.: Secondary
735 aerosol formation promotes water uptake by organic-rich wildfire haze particles in equatorial Asia,
736 *Atmos. Chem. Phys.*, 18, 7781–7798, <https://doi.org/10.5194/acp-18-7781-2018>, 2018.

737 Cheng, Y. F., Su, H., Rose, D., Gunthe, S. S., Berghof, M., Wehner, B., Achtert, P., Nowak, A.,
738 Takegawa, N., Kondo, Y., Shiraiwa, M., Gong, Y. G., Shao, M., Hu, M., Zhu, T., Zhang, Y. H.,
739 Carmichael, G. R., Wiedensohler, A., Andreae, M. O., and Pöschl, U.: Size-resolved measurement of
740 the mixing state of soot in the megacity Beijing, China: diurnal cycle, aging and parameterization,
741 *Atmos. Chem. Phys.*, 12, 4477–4491, <https://doi.org/10.5194/acp-12-4477-2012>, 2012.

742 Ching, J., Fast, J., West, M., and Riemer, N.: Metrics to quantify the importance of mixing state
743 for CCN activity, *Atmos. Chem. Phys.*, 17, 7445–7458, <https://doi.org/10.5194/acp-17-7445-2017>,
744 2017.

745 Ching, J., Adachi, K., Zaizen, Y., Igarashi, Y., and Kajino, M.: Aerosol mixing state revealed by
746 transmission electron microscopy pertaining to cloud formation and human airway deposition, *npj*
747 *Climate and Atmospheric Science*, 2, 22, <https://doi.org/10.1038/s41612-019-0081-9>, 2019.

748 Deng, Z. Z., Zhao, C. S., Ma, N., Liu, P. F., Ran, L., Xu, W. Y., Chen, J., Liang, Z., Liang, S.,
749 Huang, M. Y., Ma, X. C., Zhang, Q., Quan, J. N., Yan, P., Henning, S., Mildenberger, K., Sommerhage,
750 E., Schäfer, M., Stratmann, F., and Wiedensohler, A.: Size-resolved and bulk activation properties of
751 aerosols in the North China Plain, *Atmos. Chem. Phys.*, 11, 3835–3846, [https://doi.org/10.5194/acp-](https://doi.org/10.5194/acp-11-3835-2011)
752 11-3835-2011, 2011.

753 Deng, Z. Z., Zhao, C. S., Ma, N., Ran, L., Zhou, G. Q., Lu, D. R., and Zhou, X. J.: An examination
754 of parameterizations for the CCN number concentration based on in situ measurements of aerosol
755 activation properties in the North China Plain, *Atmos. Chem. Phys.*, 13, 6227–6237,
756 <https://doi.org/10.5194/acp-13-6227-2013>, 2013.

757 Dusek, U., Frank, G.P., et al., 2011. Water uptake by biomass burning aerosol at sub- and
758 supersaturated conditions: closure studies and implications for the role of organics. *Atmos. Chem.*
759 *Phys.* 11 (18), 9519–9532.

760 Drinovec, L., Močnik, G., Zotter, P., Prévôt, A. S. H., Ruckstuhl, C., Coz, E., Rupakheti, M.,
761 Sciare, J., Müller, T., Wiedensohler, A., and Hansen, A. D. A.: The “dual-spot” Aethalometer: an
762 improved measurement of aerosol black carbon with real-time loading compensation, *Atmos. Meas.*
763 *Tech.*, 8, 1965–1979, <https://doi.org/10.5194/amt-8-1965-2015>, 2015.

764 Engelhart, G. J., Hennigan, C. J., Miracolo, M. A., Robinson, A. L., and Pandis, S. N.: Cloud
765 condensation nuclei activity of fresh primary and aged biomass burning aerosol, *Atmos. Chem. Phys.*,
766 12, 7285–7293, <https://doi.org/10.5194/acp-12-7285-2012>, 2012.

767 Ervens, B.: Modeling the Processing of Aerosol and Trace Gases in Clouds and Fogs, *Chemical*
768 *Reviews*, 115, 4157–4198, <https://doi.org/10.1021/cr5005887>, 2015.

769 Farmer, D. K., Cappa, C. D., and Kreidenweis, S. M.: Atmospheric Processes and Their
770 Controlling Influence on Cloud Condensation Nuclei Activity, *Chemical Reviews*, 115, 4199–4217,
771 <https://doi.org/10.1021/cr5006292>, 2015.

772 Fierce, L., Riemer, N., and Bond, T. C.: Toward Reduced Representation of Mixing State for
773 Simulating Aerosol Effects on Climate, *Bulletin of the American Meteorological Society*, 98, 971–
774 980, <https://doi.org/10.1175/BAMS-D-16-0028.1>, 2017.

775 Fofie, E. A., Donahue, N. M., and Asa-Awuku, A.: Cloud condensation nuclei activity and droplet
776 formation of primary and secondary organic aerosol mixtures, *Aerosol Science and Technology*, 52,
777 242–251, <https://doi.org/10.1080/02786826.2017.1392480>, 2018.

778 Fu, Y., Peng, X., Sun, W., Hu, X., Wang, D., Yang, Y., Guo, Z., Wang, Y., Zhang, G., Zhu, J.,
779 Ou, J., Shi, Z., Wang, X., and Bi, X.: Impact of Cloud Process in the Mixing State and Microphysical
780 Properties of Soot Particles: Implications in Light Absorption Enhancement, *Journal of Geophysical
781 Research: Atmospheres*, n/a, e2022JD037169, <https://doi.org/10.1029/2022JD037169>, 2022.

782 Gysel, M., Laborde, M., Olfert, J. S., Subramanian, R., and Gröhn, A. J.: Effective density of
783 Aquadag and fullerene soot black carbon reference materials used for SP2 calibration, *Atmos. Meas.
784 Tech.*, 4, 2851–2858, <https://doi.org/10.5194/amt-4-2851-2011>, 2011.

785 Hennigan, C. J., Westervelt, D. M., Riipinen, I., Engelhart, G. J., Lee, T., Collett Jr., J. L., Pandis,
786 S. N., Adams, P. J., and Robinson, A. L.: New particle formation and growth in biomass burning
787 plumes: An important source of cloud condensation nuclei, *Geophysical Research Letters*, 39,
788 <https://doi.org/10.1029/2012GL050930>, 2012.

789 Herich, H., Kammermann, L., Gysel, M., Weingartner, E., Baltensperger, U., Lohmann, U., and
790 Cziczo, D. J.: In situ determination of atmospheric aerosol composition as a function of hygroscopic
791 growth, *Journal of Geophysical Research: Atmospheres*, 113, <https://doi.org/10.1029/2008JD009954>,
792 2008.

793 Herich, H., Kammermann, L., Friedman, B., Gross, D. S., Weingartner, E., Lohmann, U.,
794 Spichtinger, P., Gysel, M., Baltensperger, U., and Cziczo, D. J.: Subarctic atmospheric aerosol
795 composition: 2. Hygroscopic growth properties, *Journal of Geophysical Research: Atmospheres*, 114,
796 <https://doi.org/10.1029/2008JD011574>, 2009.

797 Hersey, S. P., Craven, J. S., Metcalf, A. R., Lin, J., Latham, T., Suski, K. J., Cahill, J. F., Duong,
798 H. T., Sorooshian, A., Jonsson, H. H., Shiraiwa, M., Zuend, A., Nenes, A., Prather, K. A., Flagan, R.
799 C., and Seinfeld, J. H.: Composition and hygroscopicity of the Los Angeles Aerosol: CalNex, *Journal
800 of Geophysical Research: Atmospheres*, 118, 3016–3036, <https://doi.org/10.1002/jgrd.50307>, 2013.

801 Hodas, N., Zuend, A., et al., 2016. Discontinuities in hygroscopic growth below and above water
802 saturation for laboratory surrogates of oligomers in organic atmospheric aerosols. *Atmos. Chem. Phys.
803 Discuss.* 1–34, 2016.

804 Hong, J., Äijälä, M., Häme, S. A. K., Hao, L., Duplissy, J., Heikkinen, L. M., Nie, W., Mikkilä,
805 J., Kulmala, M., Prisle, N. L., Virtanen, A., Ehn, M., Paasonen, P., Worsnop, D. R., Riipinen, I., Petäjä,
806 T., and Kerminen, V.-M.: Estimates of the organic aerosol volatility in a boreal forest using two
807 independent methods, *Atmos. Chem. Phys.*, 17, 4387–4399, [https://doi.org/10.5194/acp-17-4387-
808 2017](https://doi.org/10.5194/acp-17-4387-2017), 2017.

809 Jayne, J. T., Leard, D. C., Zhang, X., Davidovits, P., Smith, K. A., Kolb, C. E., and Worsnop, D.
810 R.: Development of an Aerosol Mass Spectrometer for Size and Composition Analysis of Submicron
811 Particles, *Aerosol Science and Technology*, 33, 49–70, <https://doi.org/10.1080/027868200410840>,
812 2000.

813 Jiang, X., Tao, J., Kuang, Y., Hong, J., and Ma, N.: Mathematical derivation and physical
814 interpretation of particle size-resolved activation ratio based on particle hygroscopicity distribution:
815 Application on global characterization of CCN activity, *Atmospheric Environment*, 246, 118137,
816 <https://doi.org/10.1016/j.atmosenv.2020.118137>, 2021.

817 Jurányi, Z., Tritscher, T., Gysel, M., Laborde, M., Gomes, L., Roberts, G., Baltensperger, U., and
818 Weingartner, E.: Hygroscopic mixing state of urban aerosol derived from size-resolved cloud
819 condensation nuclei measurements during the MEGAPOLI campaign in Paris, *Atmos. Chem. Phys.*,
820 13, 6431–6446, <https://doi.org/10.5194/acp-13-6431-2013>, 2013.

821 Kawana, K., Nakayama, T., and Mochida, M.: Hygroscopicity and CCN activity of atmospheric
822 aerosol particles and their relation to organics: Characteristics of urban aerosols in Nagoya, Japan,
823 *Journal of Geophysical Research: Atmospheres*, 121, 4100–4121,
824 <https://doi.org/10.1002/2015jd023213>, 2016.

825 Kim, N., Yum, S. S., Park, M., Park, J. S., Shin, H. J., and Ahn, J. Y.: Hygroscopicity of urban
826 aerosols and its link to size-resolved chemical composition during spring and summer in Seoul, Korea,
827 *Atmos. Chem. Phys.*, 20, 11245–11262, <https://doi.org/10.5194/acp-20-11245-2020>, 2020.

828 Kuang, Y., Zhao, C. S., Tao, J. C., and Ma, N.: Diurnal variations of aerosol optical properties in
829 the North China Plain and their influences on the estimates of direct aerosol radiative effect, *Atmos.*
830 *Chem. Phys.*, 15, 5761–5772, <https://doi.org/10.5194/acp-15-5761-2015>, 2015.

831 Kuang, Y., He, Y., Xu, W., Yuan, B., Zhang, G., Ma, Z., Wu, C., Wang, C., Wang, S., Zhang, S.,
832 Tao, J., Ma, N., Su, H., Cheng, Y., Shao, M., and Sun, Y.: Photochemical Aqueous-Phase Reactions
833 Induce Rapid Daytime Formation of Oxygenated Organic Aerosol on the North China Plain,
834 *Environmental Science & Technology*, 54, 3849–3860, <https://doi.org/10.1021/acs.est.9b06836>, 2020.

835 Kuang, Y., Huang, S., Xue, B., Luo, B., Song, Q., Chen, W., Hu, W., Li, W., Zhao, P., Cai, M.,
836 Peng, Y., Qi, J., Li, T., Wang, S., Chen, D., Yue, D., Yuan, B., and Shao, M.: Contrasting effects of
837 secondary organic aerosol formations on organic aerosol hygroscopicity, *Atmos. Chem. Phys.*, 21,
838 10375–10391, <https://doi.org/10.5194/acp-21-10375-2021>, 2021.

839 Kuwata, M. and Kondo, Y.: Dependence of size-resolved CCN spectra on the mixing state of
840 nonvolatile cores observed in Tokyo, *Journal of Geophysical Research: Atmospheres*, 113,
841 <https://doi.org/10.1029/2007JD009761>, 2008.

842 Kuwata, M., Kondo, Y., Mochida, M., Takegawa, N., and Kawamura, K.: Dependence of CCN
843 activity of less volatile particles on the amount of coating observed in Tokyo, *Journal of Geophysical*
844 *Research: Atmospheres*, 112, <https://doi.org/10.1029/2006JD007758>, 2007.

845 Laborde, M.; Crippa, M.; Tritscher, T.; Jurañyi, Z.; Decarlo, P. F.; Temime-Roussel, B.; Marchand, N.;
846 Eckhardt, S.; Stohl, A.; Baltensperger, U.; Pre v t, A.S.H.; Weingartner, E.; Gysel, M. Black carbon
847 physical properties and mixing state in the European megacity Paris. *Atmos. Chem. Phys.* 2013, 13
848 (11), 5831–5856.

849 Lack, D. A., Langridge, J. M., Bahreini, R., Cappa, C. D., Middlebrook, A. M., and Schwarz, J.
850 P.: Brown carbon and internal mixing in biomass burning particles, *Proceedings of the National*
851 *Academy of Sciences*, 109, 14802–14807, <https://doi.org/10.1073/pnas.1206575109>, 2012.

852 Lance, S., Nenes, A., Medina, J., and Smith, J. N.: Mapping the operation of the DMT continuous
853 flow CCN counter, *Aerosol science and technology*, 40, 242–254, 2006.

854 Lance, S., Raatikainen, T., Onasch, T. B., Worsnop, D. R., Yu, X. Y., Alexander, M. L.,
855 Stolzenburg, M. R., McMurry, P. H., Smith, J. N., and Nenes, A.: Aerosol mixing state, hygroscopic
856 growth and cloud activation efficiency during MIRAGE 2006, *Atmos. Chem. Phys.*, 13, 5049–5062,
857 <https://doi.org/10.5194/acp-13-5049-2013>, 2013.

858 Lata, N. N., Zhang, B., Schum, S., Mazzoleni, L., Brimberry, R., Marcus, M. A., Cantrell, W. H.,
859 Fialho, P., Mazzoleni, C., and China, S.: Aerosol Composition, Mixing State, and Phase State of Free
860 Tropospheric Particles and Their Role in Ice Cloud Formation, *ACS Earth Space Chem.*, 5, 3499–
861 3510, <https://doi.org/10.1021/acsearthspacechem.1c00315>, 2021.

862 Lee, A. K. Y., Rivellini, L.-H., Chen, C.-L., Liu, J., Price, D. J., Betha, R., Russell, L. M., Zhang,
863 X., and Cappa, C. D.: Influences of Primary Emission and Secondary Coating Formation on the
864 Particle Diversity and Mixing State of Black Carbon Particles, *Environ. Sci. Technol.*, 53, 9429–9438,
865 <https://doi.org/10.1021/acs.est.9b03064>, 2019.

866 Li, G., Su, H., Ma, N., Tao, J., Kuang, Y., Wang, Q., Hong, J., Zhang, Y., Kuhn, U., and Zhang,
867 S.: Multiphase chemistry experiment in Fogs and Aerosols in the North China Plain (McFAN):
868 integrated analysis and intensive winter campaign 2018, *Faraday Discussions*, 2021.

869 Liu, D.; Whitehead, J.; Alfarra, M. R.; Reyes-Villegas, E.; Spracklen, D. V.; Reddington, C. L.;
870 Kong, S.; Williams, P. I.; Ting, Y.-C.; Haslett, S.; Taylor, J. W.; Flynn, M. J.; Morgan, W. T.;
871 McFiggans, G.; Coe, H.; Allan, J. D. Black-carbon absorption enhancement in the atmosphere
872 determined by particle mixing state. *Nat. Geosci.* 2017, 10 (3), 184–188.

873 Liu, D., Joshi, R., Wang, J., Yu, C., Allan, J. D., Coe, H., Flynn, M. J., Xie, C., Lee, J., Squires,
874 F., Kotthaus, S., Grimmond, S., Ge, X., Sun, Y., and Fu, P.: Contrasting physical properties of black
875 carbon in urban Beijing between winter and summer, *Atmos. Chem. Phys.*, 19, 6749–6769,
876 <https://doi.org/10.5194/acp-19-6749-2019>, 2019.

877 Liu, D., Li, S., Hu, D., Kong, S., Cheng, Y., Wu, Y., Ding, S., Hu, K., Zheng, S., Yan, Q., Zheng,
878 H., Zhao, D., Tian, P., Ye, J., Huang, M., and Ding, D.: Evolution of Aerosol Optical Properties from
879 Wood Smoke in Real Atmosphere Influenced by Burning Phase and Solar Radiation, *Environ. Sci.*
880 *Technol.*, 55, 5677–5688, <https://doi.org/10.1021/acs.est.0c07569>, 2021.

881 Liu, P., Song, M., et al., 2018. Resolving the mechanisms of hygroscopic growth and cloud
882 condensation nuclei activity for organic particulate matter. *Nat. Commun.* 9.

883 Liu, P., Kaplan, J. O., Mickley, L. J., Li, Y., Chellman, N. J., Arienzo, M. M., Kodros, J. K.,
884 Pierce, J. R., Sigl, M., Freitag, J., Mulvaney, R., Curran, M. A. J., and McConnell, J. R.: Improved
885 estimates of preindustrial biomass burning reduce the magnitude of aerosol climate forcing in the
886 Southern Hemisphere, *Science Advances*, 7, 10.1126/sciadv.abc1379, 2021.

887 Liu, K., Zhang, C., Cheng, Y., Liu, C., Zhang, H., Zhang, G., Sun, X., and Mu, Y.: Serious BTEX
888 pollution in rural area of the North China Plain during winter season, *Journal of Environmental*
889 *Sciences*, 30, 186–190, <https://doi.org/10.1016/j.jes.2014.05.056>, 2015.

890 Liu, P. F., Zhao, C. S., Göbel, T., Hallbauer, E., Nowak, A., Ran, L., Xu, W. Y., Deng, Z. Z., Ma,
891 N., and Mildenerger, K.: Hygroscopic properties of aerosol particles at high relative humidity and
892 their diurnal variations in the North China Plain, *Atmos. Chem. Phys.*, 11, 3479–3494, 2011.

893 Luo, B., Kuang, Y., Huang, S., Song, Q., Hu, W., Li, W., Peng, Y., Chen, D., Yue, D., Yuan, B.,
894 and Shao, M.: Parameterizations of size distribution and refractive index of biomass burning organic
895 aerosol with black carbon content, *Atmos. Chem. Phys.*, 22, 12401–12415,
896 <https://doi.org/10.5194/acp-22-12401-2022>, 2022.

897 Ma, N., Zhao, C. S., Müller, T., Cheng, Y. F., Liu, P. F., Deng, Z. Z., Xu, W. Y., Ran, L., Nekat,
898 B., van Pinxteren, D., Gnauk, T., Müller, K., Herrmann, H., Yan, P., Zhou, X. J., and Wiedensohler,
899 A.: A new method to determine the mixing state of light absorbing carbonaceous using the measured
900 aerosol optical properties and number size distributions, *Atmos. Chem. Phys.*, 12, 2381–2397,
901 <https://doi.org/10.5194/acp-12-2381-2012>, 2012.

902 Ma, N., Zhao, C., Tao, J., Wu, Z., Kecorius, S., Wang, Z., Größ, J., Liu, H., Bian, Y., Kuang, Y.,
903 Teich, M., Spindler, G., Müller, K., van Pinxteren, D., Herrmann, H., Hu, M., and Wiedensohler, A.:
904 Variation of CCN activity during new particle formation events in the North China Plain, *Atmos. Chem.*
905 *Phys.*, 16, 8593–8607, <https://doi.org/10.5194/acp-16-8593-2016>, 2016.

906 Malek, K. A., Gohil, K., Al-Abadleh, H. A., and Asa-Awuku, A. A.: Hygroscopicity of
907 polycatechol and polyguaiacol secondary organic aerosol in sub- and supersaturated water vapor
908 environments††Electronic supplementary information (ESI) available: Detailed experimental
909 procedures, and figures and tables showing data analysis. See DOI: 10.1039/d1ea00063b,
910 *Environmental Science: Atmospheres*, 2, 24–33, <https://doi.org/10.1039/d1ea00063b>, 2022.

911 May, A. A., Levin, E. J. T., Hennigan, C. J., Riipinen, I., Lee, T., Collett Jr., J. L., Jimenez, J. L.,
912 Kreidenweis, S. M., and Robinson, A. L.: Gas-particle partitioning of primary organic aerosol
913 emissions: 3. Biomass burning, *Journal of Geophysical Research: Atmospheres*, 118, 11,327–11,338,
914 <https://doi.org/10.1002/jgrd.50828>, 2013.

915 Matsui, H., Hamilton, D. S., and Mahowald, N. M.: Black carbon radiative effects highly sensitive
916 to emitted particle size when resolving mixing-state diversity, *Nature Communications*, 9, 3446,
917 <https://doi.org/10.1038/s41467-018-05635-1>, 2018.

918 Mei, F., Hayes, P. L., Ortega, A., Taylor, J. W., Allan, J. D., Gilman, J., Kuster, W., de Gouw, J.,
919 Jimenez, J. L., and Wang, J.: Droplet activation properties of organic aerosols observed at an urban
920 site during CalNex-LA, *Journal of Geophysical Research-Atmospheres*, 118, 2903–2917,
921 <https://doi.org/10.1002/jgrd.50285>, 2013.

922 Metcalf, A. R., Craven, J. S., Ensberg, J. J., Brioude, J., Angevine, W., Sorooshian, A., Duong,
923 H. T., Jonsson, H. H., Flagan, R. C., and Seinfeld, J. H.: Black carbon aerosol over the Los Angeles
924 Basin during CalNex, *Journal of Geophysical Research: Atmospheres*, 117,
925 <https://doi.org/10.1029/2011JD017255>, 2012.

926 Middlebrook, A. M., Bahreini, R., Jimenez, J. L., and Canagaratna, M. R.: Evaluation of
927 Composition-Dependent Collection Efficiencies for the Aerodyne Aerosol Mass Spectrometer using
928 Field Data, *Aerosol Science and Technology*, 46, 258–271,
929 <https://doi.org/10.1080/02786826.2011.620041>, 2012.

930 Moffet, R. C., O'Brien, R. E., Alpert, P. A., Kelly, S. T., Pham, D. Q., Gilles, M. K., Knopf, D.
931 A., and Laskin, A.: Morphology and mixing of black carbon particles collected in central California
932 during the CARES field study, *Atmos. Chem. Phys.*, 16, 14515–14525, [https://doi.org/10.5194/acp-](https://doi.org/10.5194/acp-16-14515-2016)
933 [16-14515-2016](https://doi.org/10.5194/acp-16-14515-2016), 2016.

934 Mohr, C., Huffman, J. A., Cubison, M. J., Aiken, A. C., Docherty, K. S., Kimmel, J. R., Ulbrich,
935 I. M., Hannigan, M., and Jimenez, J. L.: Characterization of Primary Organic Aerosol Emissions from
936 Meat Cooking, Trash Burning, and Motor Vehicles with High-Resolution Aerosol Mass Spectrometry
937 and Comparison with Ambient and Chamber Observations, *Environ. Sci. Technol.*, 43, 2443–2449,
938 <https://doi.org/10.1021/es8011518>, 2009.

939 Moteki, N. and Kondo, Y.: Effects of Mixing State on Black Carbon Measurements by Laser-
940 Induced Incandescence, *Aerosol Science and Technology*, 41, 398–417,
941 <https://doi.org/10.1080/02786820701199728>, 2007.

942 Mukherjee, S., Anil Kumar, V., Patil, R. D., Meena, G. S., Buchunde, P., Waghmare, V.,
943 Deshmukh, S., Dhavale, V., Ray, A., Panicker, A. S., Sonbawne, S. M., Safai, P. D., and Pandithurai,
944 G.: Investigation of physico-chemical characteristics and associated CCN activation for different
945 combustion sources through Chamber experiment approach, *Atmospheric Environment*, 266, 118726,
946 <https://doi.org/10.1016/j.atmosenv.2021.118726>, 2021.

947 Nordmann, S., Cheng, Y. F., Carmichael, G. R., Yu, M., Denier van der Gon, H. A. C., Zhang,
948 Q., Saide, P. E., Pöschl, U., Su, H., Birmili, W., and Wiedensohler, A.: Atmospheric black carbon and
949 warming effects influenced by the source and absorption enhancement in central Europe, *Atmos. Chem.*
950 *Phys.*, 14, 12683–12699, <https://doi.org/10.5194/acp-14-12683-2014>, 2014.

951 Ovadnevaite, J., Zuend, A., Laaksonen, A., Sanchez, K.J., Roberts, G., Ceburnis, D., Decesari,
952 S., Rinaldi, M., Hodas, N., Facchini, M.C., Seinfeld, J.H., O' Dowd, C., 2017. Surface tension prevails
953 over solute effect in organic-influenced cloud droplet activation. *Nature* 546, 637–641.
954 <https://doi.org/10.1038/nature22806>.

955 Paatero, P. and Tapper, U.: Positive matrix factorization: A non-negative factor model with
956 optimal utilization of error estimates of data values, *Environmetrics*, 5, 111–126,
957 <https://doi.org/10.1002/env.3170050203>, 1994.

958 Pajunoja, A., Lambe, A.T., Hakala, J., Rastak, N., Cummings, M.J., Brogan, J.F., Hao, L.,
959 Paramonov, M., Hong, J., Prisle, N.L., Malila, J., Romakkaniemi, S., Lehtinen, K.E.J., Laaksonen, A.,
960 Kulmala, M., Massoli, P., Onasch, T.B., Donahue, N.M., Riipinen, I., Davidovits, P., Worsnop, D.R.,
961 Petäjä, T., Virtanen, A., 2015. Adsorptive uptake of water by semisolid secondary organic aerosols.
962 *Geophys. Res. Lett.* 42, 3063–3068. <https://doi.org/10.1002/2015GL063142>.

963 Peng, J., Hu, M., Guo, S., Du, Z., Zheng, J., Shang, D., Levy Zamora, M., Zeng, L., Shao, M.,
964 Wu, Y.-S., Zheng, J., Wang, Y., Glen, C. R., Collins, D. R., Molina, M. J., and Zhang, R.: Markedly
965 enhanced absorption and direct radiative forcing of black carbon under polluted urban environments,

966 Proceedings of the National Academy of Sciences, 113, 4266–4271,
967 <https://doi.org/10.1073/pnas.1602310113>, 2016.

968 Pöhlker, M. L., Ditas, F., Saturno, J., Klimach, T., Hrabě de Angelis, I., Araùjo, A. C., Brito, J.,
969 Carbone, S., Cheng, Y., Chi, X., Ditz, R., Gunthe, S. S., Holanda, B. A., Kandler, K., Kesselmeier, J.,
970 Könemann, T., Krüger, O. O., Lavrič, J. V., Martin, S. T., Mikhailov, E., Moran-Zuloaga, D., Rizzo,
971 L. V., Rose, D., Su, H., Thalman, R., Walter, D., Wang, J., Wolff, S., Barbosa, H. M. J., Artaxo, P.,
972 Andreae, M. O., Pöschl, U., and Pöhlker, C.: Long-term observations of cloud condensation nuclei
973 over the Amazon rain forest – Part 2: Variability and characteristics of biomass burning, long-range
974 transport, and pristine rain forest aerosols, *Atmos. Chem. Phys.*, 18, 10289–10331,
975 <https://doi.org/10.5194/acp-18-10289-2018>, 2018.

976 Pöhlker, M. L., Pöhlker, C., Quaas, J., Mülmenstädt, J., Pozzer, A., Andreae, M. O., Artaxo, P.,
977 Block, K., Coe, H., Ervens, B., Gallimore, P., Gaston, C. J., Gunthe, S. S., Henning, S., Herrmann, H.,
978 Krüger, O. O., McFiggans, G., Poulain, L., Raj, S. S., Reyes-Villegas, E., Royer, H. M., Walter, D.,
979 Wang, Y., and Pöschl, U.: Global organic and inorganic aerosol hygroscopicity and its effect on
980 radiative forcing, *Nature communications*, 14, 6139, [10.1038/s41467-023-41695-8](https://doi.org/10.1038/s41467-023-41695-8), 2023

981 Philippin, S., Wiedensohler, A., and Stratmann, F.: Measurements of non-volatile fractions of
982 pollution aerosols with an eight-tube volatility tandem differential mobility analyzer (VTDMA-8),
983 *Journal of Aerosol Science*, 35, 185–203, <https://doi.org/10.1016/j.jaerosci.2003.07.004>, 2004.

984 Qiu, Y., Xie, Q., Wang, J., Xu, W., Li, L., Wang, Q., Zhao, J., Chen, Y., Chen, Y., Wu, Y., Du,
985 W., Zhou, W., Lee, J., Zhao, C., Ge, X., Fu, P., Wang, Z., Worsnop, D. R., and Sun, Y.: Vertical
986 Characterization and Source Apportionment of Water-Soluble Organic Aerosol with High-resolution
987 Aerosol Mass Spectrometry in Beijing, China, *ACS Earth Space Chem.*, 3, 273–284,
988 <https://doi.org/10.1021/acsearthspacechem.8b00155>, 2019.

989 Ren, J., Zhang, F., Wang, Y., Collins, D., Fan, X., Jin, X., Xu, W., Sun, Y., Cribb, M., and Li, Z.:
990 Using different assumptions of aerosol mixing state and chemical composition to predict CCN
991 concentrations based on field measurements in urban Beijing, *Atmospheric Chemistry and Physics*,
992 18, 6907–6921, <https://doi.org/10.5194/acp-18-6907-2018>, 2018.

993 Riemer, N., Ault, A. P., West, M., Craig, R. L., and Curtis, J. H.: Aerosol Mixing State:
994 Measurements, Modeling, and Impacts, *Reviews of Geophysics*, 57, 187–249,
995 <https://doi.org/10.1029/2018RG000615>, 2019.

996 Roberts, G. C. and Nenes, A.: A continuous-flow streamwise thermal-gradient CCN chamber for
997 atmospheric measurements, *Aerosol science and technology*, 39, 206–221, 2005.

998 Rose, D., Gunthe, S. S., Mikhailov, E., Frank, G. P., Dusek, U., Andreae, M. O., and Pöschl, U.:
999 Calibration and measurement uncertainties of a continuous-flow cloud condensation nuclei counter
1000 (DMT-CCNC): CCN activation of ammonium sulfate and sodium chloride aerosol particles in theory
1001 and experiment, *Atmos. Chem. Phys.*, 8, 1153–1179, 2008.

1002 Rose, D., Nowak, A., Achtert, P., Wiedensohler, A., Hu, M., Shao, M., Zhang, Y., Andreae, M.
1003 O., and Pöschl, U.: Cloud condensation nuclei in polluted air and biomass burning smoke near the
1004 mega-city Guangzhou, China - Part 1: Size-resolved measurements and implications for the modeling
1005 of aerosol particle hygroscopicity and CCN activity, *Atmos. Chem. Phys.*, 10, 3365–3383, 2010.

1006 Rose, D., Gunthe, S. S., Su, H., Garland, R. M., Yang, H., Berghof, M., Cheng, Y. F., Wehner,
1007 B., Achtert, P., Nowak, A., Wiedensohler, A., Takegawa, N., Kondo, Y., Hu, M., Zhang, Y., Andreae,
1008 M. O., and Poschl, U.: Cloud condensation nuclei in polluted air and biomass burning smoke near the
1009 mega-city Guangzhou, China -Part 2: Size-resolved aerosol chemical composition, diurnal cycles, and
1010 externally mixed weakly CCN-active soot particles, *Atmos. Chem. Phys.*, 11, 2817–2836,
1011 <https://doi.org/10.5194/acp-11-2817-2011>, 2011.

1012 Ruehl, C.R., Davies, J.F., Wilson, K.R., 2016. An interfacial mechanism for cloud droplet
1013 formation on organic aerosols. *Science* 351, 1447–1450, 6280.

1014 Saha, P. K., Khlystov, A., and Grieshop, A. P.: Downwind evolution of the volatility and mixing
1015 state of near-road aerosols near a US interstate highway, *Atmos. Chem. Phys.*, 18, 2139–2154,
1016 <https://doi.org/10.5194/acp-18-2139-2018>, 2018.

1017 Schwarz, J. P.; Gao, R. S.; Spackman, J. R.; Watts, L. A.; Thomson, D. S.; Fahey, D. W.; Ryerson,
1018 T. B.; Peischl, J.; Holloway, J. S.; Trainer, M.; Frost, G. J.; Baynard, T.; Lack, D. A.; de Gouw, J. A.;
1019 Warneke, C.; Del Negro, L. A. Measurement of the mixing state, mass, and optical size of individual
1020 black carbon particles in urban and biomass burning emissions. *Geophys. Res. Lett.* 2008, 35, L13810.

1021 Sedlacek, A. J., Lewis, E. R., Kleinman, L., Xu, J., and Zhang, Q.: Determination of and evidence
1022 for non-core-shell structure of particles containing black carbon using the Single-Particle Soot
1023 Photometer (SP2), *Geophysical Research Letters*, 39, L06802, <https://doi.org/10.1029/2012GL050905>,
1024 2012.

1025 Shi, J., Hong, J., Ma, N., Luo, Q., He, Y., Xu, H., Tan, H., Wang, Q., Tao, J., Zhou, Y., Han, S.,
1026 Peng, L., Xie, L., Zhou, G., Xu, W., Sun, Y., Cheng, Y., and Su, H.: Measurement report: On the
1027 difference in aerosol hygroscopicity between high and low relative humidity conditions in the North
1028 China Plain, *Atmos. Chem. Phys.*, 22, 4599–4613, <https://doi.org/10.5194/acp-22-4599-2022>, 2022.

1029 Spracklen, D. V., Carslaw, K. S., Pošchl, U., Rap, A., and Forster, P. M.: Global cloud
1030 condensation nuclei influenced by carbonaceous combustion aerosol, *Atmos. Chem. Phys.*, 11, 9067–
1031 9087, [doi:10.5194/acp-11-9067-2011](https://doi.org/10.5194/acp-11-9067-2011), 2011.

1032 Stevens, R., Ryjkov, A., Majdzadeh, M., and Dastoor, A.: An improved representation of aerosol
1033 mixing state for air quality–weather interactions, *Atmos. Chem. Phys.*, 22, 13527–13549,
1034 <https://doi.org/10.5194/acp-22-13527-2022>, 2022.

1035 Stolzenburg, M. R. and McMurry, P. H.: Equations governing single and tandem DMA
1036 configurations and a new lognormal approximation to the transfer function, *Aerosol Science and
1037 Technology*, 42, 421–432, 2008.

1038 Su, H., Rose, D., Cheng, Y. F., Gunthe, S. S., Massling, A., Stock, M., Wiedensohler, A., Andreae,
1039 M. O., and Poschl, U.: Hygroscopicity distribution concept for measurement data analysis and
1040 modeling of aerosol particle mixing state with regard to hygroscopic growth and CCN activation,
1041 *Atmos. Chem. Phys.*, 10, 7489–7503, <https://doi.org/10.5194/acp-10-7489-2010>, 2010.

1042 Subramanian, R., Kok, G. L., Baumgardner, D., Clarke, A., Shinozuka, Y., Campos, T. L., Heizer,
1043 C. G., Stephens, B. B., de Foy, B., Voss, P. B., and Zaveri, R. A.: Black carbon over Mexico: the effect
1044 of atmospheric transport on mixing state, mass absorption cross-section, and BC/CO ratios, *Atmos.
1045 Chem. Phys.*, 10, 219–237, <https://doi.org/10.5194/acp-10-219-2010>, 2010.

1046 Tan, H., Xu, H., Wan, Q., Li, F., Deng, X., Chan, P. W., Xia, D., and Yin, Y.: Design and
1047 Application of an Unattended Multifunctional H-TDMA System, *Journal of Atmospheric and Oceanic*
1048 *Technology*, 30, 1136–1148, <https://doi.org/10.1175/JTECH-D-12-00129.1>, 2013.

1049 Tao, J., Zhao, C., Nan, M., and Ye, K.: Consistency and applicability of parameterization schemes
1050 for the size-resolved aerosol activation ratio based on field measurements in the North China Plain,
1051 *Atmospheric Environment*, 173, 316–324, 2018.

1052 Tao, J., Kuang, Y., Ma, N., Zheng, Y., Wiedensohler, A., and Zhao, C.: An improved
1053 parameterization scheme for size-resolved particle activation ratio and its application on comparison
1054 study of particle hygroscopicity measurements between HTDMA and DMA-CCNC, *Atmospheric*
1055 *Environment*, 226, 117403, <https://doi.org/10.1016/j.atmosenv.2020.117403>, 2020.

1056 Tao, J., Kuang, Y., Ma, N., Hong, J., Sun, Y., Xu, W., Zhang, Y., He, Y., Luo, Q., Xie, L., Su,
1057 H., and Cheng, Y.: Secondary aerosol formation alters CCN activity in the North China Plain, *Atmos.*
1058 *Chem. Phys.*, 21, 7409–7427, <https://doi.org/10.5194/acp-21-7409-2021>, 2021.

1059 Tao, M., Chen, L., Su, L., and Tao, J.: Satellite observation of regional haze pollution over the
1060 North China Plain, *Journal of Geophysical Research: Atmospheres*, 117,
1061 <https://doi.org/10.1029/2012JD017915>, 2012.

1062 Thalman, R., de Sa, S. S., Palm, B. B., Barbosa, H. M. J., Poehlker, M. L., Alexander, M. L.,
1063 Brito, J., Carbone, S., Castillo, P., Day, D. A., Kuang, C., Manzi, A., Ng, N. L., Sedlacek, A. J., Souza,
1064 R., Springston, S., Watson, T., Poehlker, C., Poeschl, U., Andreae, M. O., Artaxo, P., Jimenez, J. L.,
1065 Martin, S. T., and Wang, J.: CCN activity and organic hygroscopicity of aerosols downwind of an
1066 urban region in central Amazonia: seasonal and diel variations and impact of anthropogenic emissions,
1067 *Atmospheric Chemistry and Physics*, 17, 11779–11801, <https://doi.org/10.5194/acp-17-11779-2017>,
1068 2017.

1069 Ting, Y., Mitchell, E. J. S., Allan, J. D., Liu, D., Spracklen, D. V., Williams, A., Jones, J. M.,
1070 Lea-Langton, A. R., McFiggans, G., and Coe, H.: Mixing State of Carbonaceous Aerosols of Primary
1071 Emissions from “Improved” African Cookstoves, *Environ. Sci. Technol.*, 52, 10134–10143,
1072 <https://doi.org/10.1021/acs.est.8b00456>, 2018.

1073 Tomlin, J. M., Jankowski, K. A., Veghte, D. P., China, S., Wang, P., Fraund, M., Weis, J., Zheng,
1074 G., Wang, Y., Rivera-Adorno, F., Raveh-Rubin, S., Knopf, D. A., Wang, J., Gilles, M. K., Moffet, R.
1075 C., and Laskin, A.: Impact of dry intrusion events on the composition and mixing state of particles
1076 during the winter Aerosol and Cloud Experiment in the Eastern North Atlantic (ACE-ENA), *Atmos.*
1077 *Chem. Phys.*, 21, 18123–18146, <https://doi.org/10.5194/acp-21-18123-2021>, 2021.

1078 Ulbrich, I. M., Canagaratna, M. R., Zhang, Q., Worsnop, D. R., and Jimenez, J. L.: Interpretation
1079 of organic components from Positive Matrix Factorization of aerosol mass spectrometric data, *Atmos.*
1080 *Chem. Phys.*, 9, 2891–2918, <https://doi.org/10.5194/acp-9-2891-2009>, 2009.

1081 Vu, D., Short, D., Karavalakis, G., Durbin, T. D., and Asa-Awuku, A.: Integrating Cloud
1082 Condensation Nuclei Predictions with Fast Time Resolved Aerosol Instrumentation to Determine the
1083 Hygroscopic Properties of Emissions Over Transient Drive Cycles, *Aerosol Science and Technology*,
1084 49, 1149–1159, <https://doi.org/10.1080/02786826.2015.1105358>, 2015.

1085 Vu, D., Short, D., Karavalakis, G., Durbin, T. D., and Asa-Awuku, A.: Will Aerosol
1086 Hygroscopicity Change with Biodiesel, Renewable Diesel Fuels and Emission Control Technologies?,
1087 *Environ. Sci. Technol.*, 51, 1580–1586, <https://doi.org/10.1021/acs.est.6b03908>, 2017.

1088 Wang, X., Ye, X., Chen, J., Wang, X., Yang, X., Fu, T.-M., Zhu, L., and Liu, C.: Direct links
1089 between hygroscopicity and mixing state of ambient aerosols: estimating particle hygroscopicity from
1090 their single-particle mass spectra, *Atmos. Chem. Phys.*, 20, 6273–6290, [https://doi.org/10.5194/acp-](https://doi.org/10.5194/acp-20-6273-2020)
1091 [20-6273-2020](https://doi.org/10.5194/acp-20-6273-2020), 2020.

1092 Wang, Y., Wang, X., Kondo, Y., Kajino, M., Munger, J. W., and Hao, J.: Black carbon and its
1093 correlation with trace gases at a rural site in Beijing: Top-down constraints from ambient
1094 measurements on bottom-up emissions, *Journal of Geophysical Research: Atmospheres*, 116,
1095 <https://doi.org/10.1029/2011JD016575>, 2011.

1096 Wang, Y., Zhang, F., Li, Z., Tan, H., Xu, H., Ren, J., Zhao, J., Du, W., and Sun, Y.: Enhanced
1097 hydrophobicity and volatility of submicron aerosols under severe emission control conditions in
1098 Beijing, *Atmos. Chem. Phys.*, 17, 5239–5251, <https://doi.org/10.5194/acp-17-5239-2017>, 2017.

1099 Wang, Y., Hu, R., Wang, Q., Li, Z., Cribb, M., Sun, Y., Song, X., Shang, Y., Wu, Y., Huang, X.,
1100 and Wang, Y.: Different effects of anthropogenic emissions and aging processes on the mixing state
1101 of soot particles in the nucleation and accumulation modes, *Atmos. Chem. Phys.*, 22, 14133–14146,
1102 <https://doi.org/10.5194/acp-22-14133-2022>, 2022.

1103 Wehner, B., Berghof, M., Cheng, Y. F., Achtert, P., Birmili, W., Nowak, A., Wiedensohler, A.,
1104 Garland, R. M., Pöschl, U., Hu, M., and Zhu, T.: Mixing state of nonvolatile aerosol particle fractions
1105 and comparison with light absorption in the polluted Beijing region, *Journal of Geophysical Research:*
1106 *Atmospheres*, 114, <https://doi.org/10.1029/2008JD010923>, 2009.

1107 Wex, H., Petters, M.D., et al., 2009. Towards closing the gap between hygroscopic growth and
1108 activation for secondary organic aerosol: Part 1-Evidence from measurements. *Atmos. Chem. Phys.* 9
1109 (12), 3987–3997.

1110 Wu, Y., Wang, X., Tao, J., Huang, R., Tian, P., Cao, J., Zhang, L., Ho, K.-F., Han, Z., and Zhang,
1111 R.: Size distribution and source of black carbon aerosol in urban Beijing during winter haze episodes,
1112 *Atmos. Chem. Phys.*, 17, 7965–7975, <https://doi.org/10.5194/acp-17-7965-2017>, 2017.

1113 Xu, W., Sun, Y., Wang, Q., Zhao, J., Wang, J., Ge, X., Xie, C., Zhou, W., Du, W., Li, J., Fu, P.,
1114 Wang, Z., Worsnop, D. R., and Coe, H.: Changes in Aerosol Chemistry From 2014 to 2016 in Winter
1115 in Beijing: Insights From High-Resolution Aerosol Mass Spectrometry, *Journal of Geophysical*
1116 *Research: Atmospheres*, 124, 1132–1147, <https://doi.org/10.1029/2018JD029245>, 2019.

1117 Xu, W. Y., Zhao, C. S., Ran, L., Deng, Z. Z., Liu, P. F., Ma, N., Lin, W. L., Xu, X. B., Yan, P.,
1118 He, X., Yu, J., Liang, W. D., and Chen, L. L.: Characteristics of pollutants and their correlation to
1119 meteorological conditions at a suburban site in the North China Plain, *Atmos. Chem. Phys.*, 11, 4353–
1120 4369, <https://doi.org/10.5194/acp-11-4353-2011>, 2011.

1121 Yang, Z., Ma, N., Wang, Q., Li, G., Pan, X., Dong, W., Zhu, S., Zhang, S., Gao, W., He, Y., Xie,
1122 L., Zhang, Y., Kuhn, U., Xu, W., Kuang, Y., Tao, J., Hong, J., Zhou, G., Sun, Y., Su, H., and Cheng,
1123 Y.: Characteristics and source apportionment of black carbon aerosol in the North China Plain,
1124 *Atmospheric Research*, 276, 106246, <https://doi.org/10.1016/j.atmosres.2022.106246>, 2022.

1125 Zhang, F., Li, Y., Li, Z., Sun, L., Li, R., Zhao, C., Wang, P., Sun, Y., Liu, X., Li, J., Li, P., Ren,
1126 G., and Fan, T.: Aerosol hygroscopicity and cloud condensation nuclei activity during the AC3Exp
1127 campaign: implications for cloud condensation nuclei parameterization, *Atmos. Chem. Phys.*, 14,
1128 13423–13437, <https://doi.org/10.5194/acp-14-13423-2014>, 2014.

1129 Zhang, F., Wang, Y., Peng, J., Chen, L., Sun, Y., Duan, L., Ge, X., Li, Y., Zhao, J., Liu, C., Zhang,
1130 X., Zhang, G., Pan, Y., Wang, Y., Zhang, A. L., Ji, Y., Wang, G., Hu, M., Molina, M. J., and Zhang,
1131 R.: An unexpected catalyst dominates formation and radiative forcing of regional haze, *Proceedings
1132 of the National Academy of Sciences*, 117, 3960–3966, <https://doi.org/10.1073/pnas.1919343117>,
1133 2020.

1134 Zhang, G., Fu, Y., Peng, X., Sun, W., Shi, Z., Song, W., Hu, W., Chen, D., Lian, X., Li, L., Tang,
1135 M., Wang, X., and Bi, X.: Black Carbon Involved Photochemistry Enhances the Formation of Sulfate
1136 in the Ambient Atmosphere: Evidence From In Situ Individual Particle Investigation, *Journal of
1137 Geophysical Research: Atmospheres*, 126, e2021JD035226, <https://doi.org/10.1029/2021JD035226>,
1138 2021.

1139 Zhang, S., Shen, X., Sun, J., Zhang, Y., Zhang, X., Xia, C., Hu, X., Zhong, J., Wang, J., and Liu,
1140 S.: Atmospheric Particle Hygroscopicity and the Influence by Oxidation State of Organic Aerosols in
1141 Urban Beijing, *Journal of Environmental Sciences*, 124, 544–556,
1142 <https://doi.org/10.1016/j.jes.2021.11.019>, 2023.

1143 Zhang, S. L., Ma, N., Kecorius, S., Wang, P. C., Hu, M., Wang, Z. B., Größ, J., Wu, Z. J., and
1144 Wiedensohler, A.: Mixing state of atmospheric particles over the North China Plain, *Atmospheric
1145 Environment*, 125, 152–164, 2016.

1146 Zhang, Y., Su, H., Ma, N., Li, G., Kecorius, S., Wang, Z., Hu, M., Zhu, T., He, K., Wiedensohler,
1147 A., Zhang, Q., and Cheng, Y.: Sizing of Ambient Particles From a Single-Particle Soot Photometer
1148 Measurement to Retrieve Mixing State of Black Carbon at a Regional Site of the North China Plain,
1149 *Journal of Geophysical Research: Atmospheres*, 123, 12,778–12,795,
1150 <https://doi.org/10.1029/2018JD028810>, 2018.

1151 Zhang, Y., Yuan, Q., Huang, D., Kong, S., Zhang, J., Wang, X., Lu, C., Shi, Z., Zhang, X., Sun,
1152 Y., Wang, Z., Shao, L., Zhu, J., and Li, W.: Direct Observations of Fine Primary Particles From
1153 Residential Coal Burning: Insights Into Their Morphology, Composition, and Hygroscopicity, *Journal
1154 of Geophysical Research: Atmospheres*, 123, 12,964–12,979, <https://doi.org/10.1029/2018JD028988>,
1155 2018.

1156 Zhang, Y., Zhang, Q., Yao, Z., & Li, H. (2020). Particle Size and Mixing State of Freshly Emitted
1157 Black Carbon from Different Combustion Sources in China. *Environmental Science & Technology*,
1158 54(13), 7766–7774. <https://doi.org/10.1021/acs.est.9b07373>

1159 Zhao, G., Tao, J., Kuang, Y., Shen, C., Yu, Y., and Zhao, C.: Role of black carbon mass size
1160 distribution in the direct aerosol radiative forcing, *Atmos. Chem. Phys.*, 19, 13175–13188,
1161 <https://doi.org/10.5194/acp-19-13175-2019>, 2019.

1162 Zhao, G., Tan, T., Hu, S., Du, Z., Shang, D., Wu, Z., Guo, S., Zheng, J., Zhu, W., Li, M., Zeng,
1163 L., and Hu, M.: Mixing state of black carbon at different atmospheres in north and southwest China,
1164 *Atmos. Chem. Phys.*, 22, 10861–10873, <https://doi.org/10.5194/acp-22-10861-2022>, 2022.

1165 Zheng, H., Kong, S., Wu, F., Cheng, Y., Niu, Z., Zheng, S., Yang, G., Yao, L., Yan, Q., Wu, J.,
1166 Zheng, M., Chen, N., Xu, K., Yan, Y., Liu, D., Zhao, D., Zhao, T., Bai, Y., Li, S., and Qi, S.: Intra-
1167 regional transport of black carbon between the south edge of the North China Plain and central China
1168 during winter haze episodes, *Atmos. Chem. Phys.*, 19, 4499–4516, [https://doi.org/10.5194/acp-19-](https://doi.org/10.5194/acp-19-4499-2019)
1169 4499-2019, 2019.

1170 Zhuang, B. L., Li, S., Wang, T. J., Deng, J. J., Xie, M., Yin, C. Q., and Zhu, J. L.: Direct radiative
1171 forcing and climate effects of anthropogenic aerosols with different mixing states over China,
1172 *Atmospheric Environment*, 79, 349–361, <https://doi.org/10.1016/j.atmosenv.2013.07.004>, 2013.

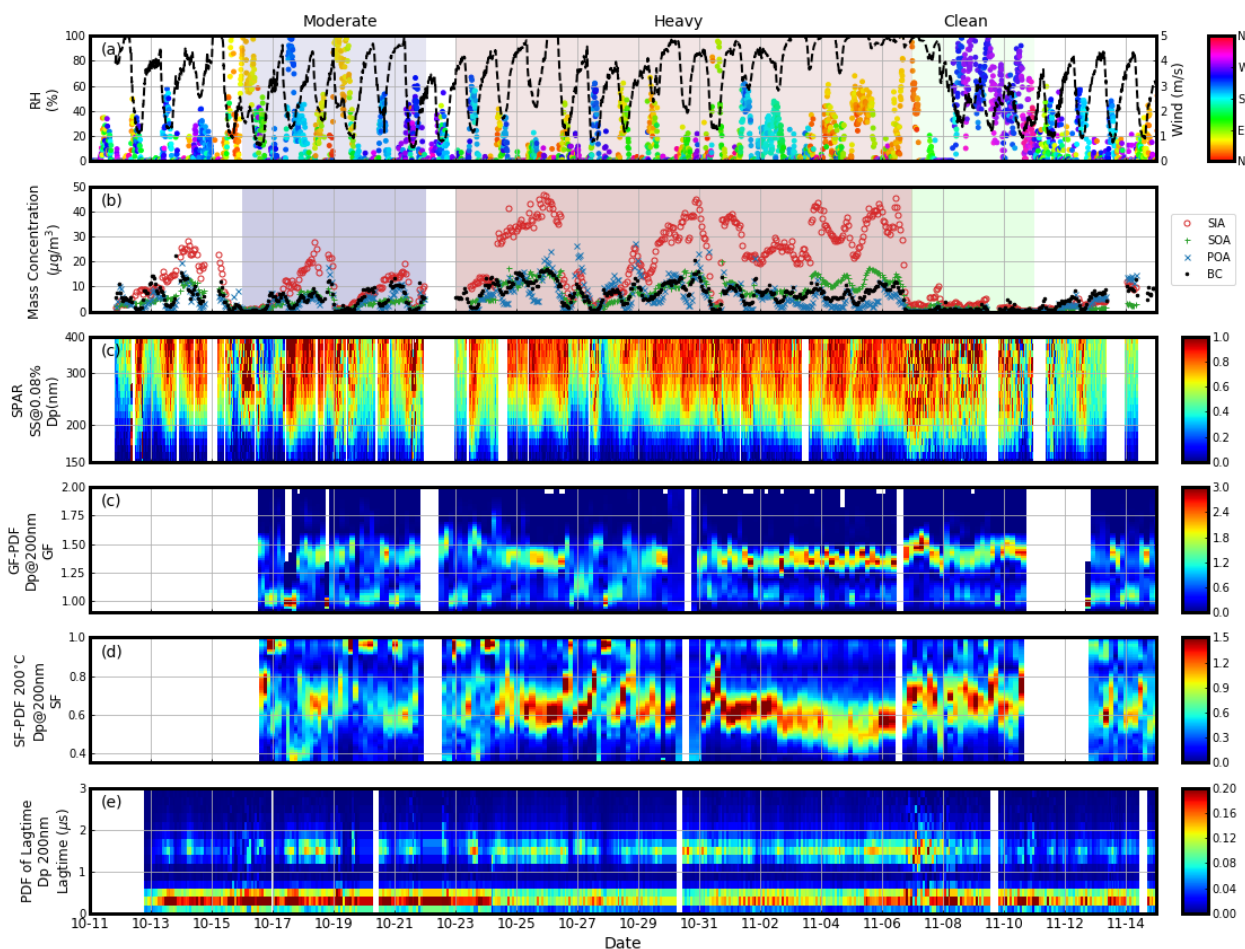
Table 1. Definition and description of abbreviations.

Abbreviation	Full name and/or Definition
	Biomass Burning Organic Aerosol
BBOA	Characterized by obvious m/z 60 (mainly C ₂ H ₄ O ₂ ⁺) and 73 (mainly C ₃ H ₅ O ₂ ⁺), which are two indicators of biomass burning
	Midpoint activation diameter
D_a	Linked to the hygroscopicity of CCNs
	Particle diameter under dry conditions without humidification or heating
D_d	
	Particle diameter after humidification or heating
D_p	
	Growth factor
GF	The ratio between particles with and without humidification and is linked to aerosol hygroscopicity
κ	Hygroscopicity parameter
MF	Mass Fraction
	Maximum Activation Fraction
MAF	An asymptote of the measured SPAR curve at large particle sizes and represents the number fraction of CCNs to total particles
NF _H	Number Fraction of Hydrophilic aerosol whose hygroscopicity parameter is $> \sim 0.07$ at particle size of 50, 100, 150 and 200 nm
NF _V	Number Fraction of Volatile aerosol whose Shrinkage Factor at 200 °C is < 0.85 at particle size of 50, 100, 150 and 200 nm
NF _{noBC}	Number Fraction of black carbon (BC)-free particles at particle size of 200, 250, 300 and 370 nm
NF _{CBC}	Number Fraction of thickly coated BC particles at particle size of 200, 250, 300 and 370 nm
NF _A -NF _B (NF _{noBC} -NF _H , NF _V -NF _H , NF _{noBC} -NF _V , NF _V -MAF,	The difference between the number fraction of A and B at particle size of 200 nm

NF _{noBC} -MAF)	
OOA1 and OOA2	Two OOA factors resolved from the PMF analysis
PDF	Probability Distribution Function
PM _{2.5}	Particulate Matter with an aerodynamic diameter <2.5 μm
PM ₁	Particulate Matter with an aerodynamic diameter <1 μm
POA	Primary Organic Aerosol Summation of BBOA and FFOA
R _{exBC}	The number concentration ratio of externally mixed BC particles in total BC-containing particles Externally mixed BC particles are defined as identified bare/thinly coated BC-containing particles at particle size of 200, 250, 300 and 370 nm
SA	Secondary Aerosols, including nitrate, sulfate, ammonium and the two OOA factors
SF	Shrinkage Factor The ratio between particles with and without heating and is linked to aerosol volatility
SIA	Secondary Inorganic Aerosols, including nitrate, sulfate, and ammonium
SOA	Secondary Organic Aerosols, including the two OOA factors
SPAR	Size-resolved Particle Activation Ratio Size-dependent CCN activity under a specific SS

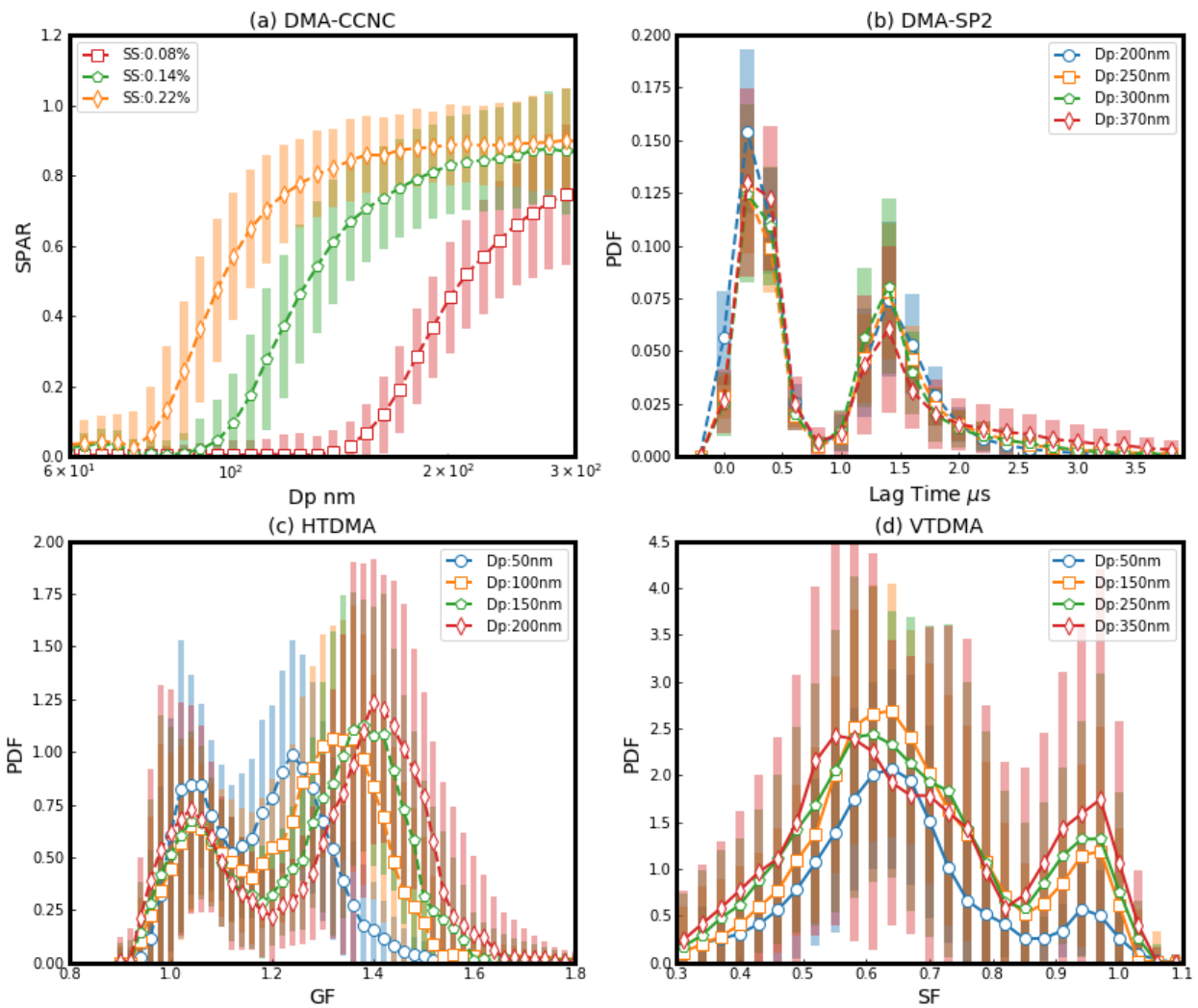
1174

1175



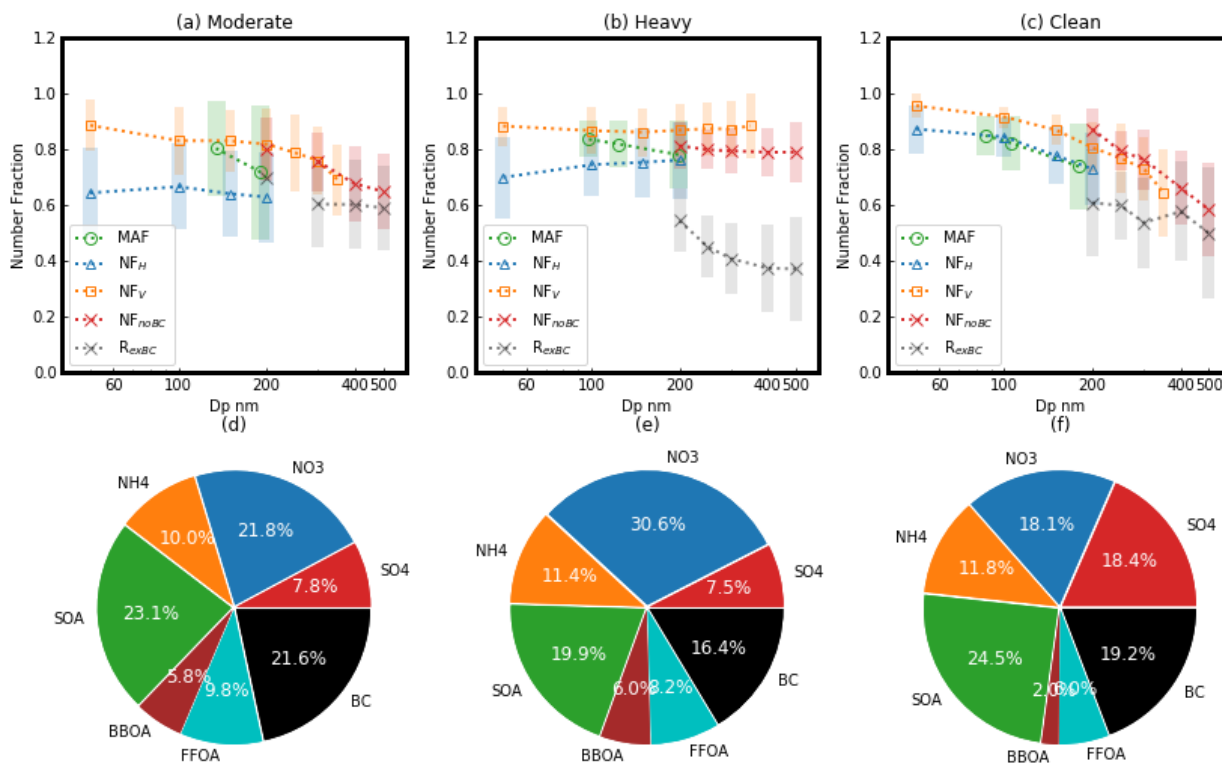
1176

1177 **Figure 1.** Overview of the measurements during the campaign: **(a)** meteorological parameters: wind speed (dots) and
 1178 relative humidity (RH) (black line), with colors of dots representing wind direction; **(b)** mass concentrations of
 1179 aerosol chemical components: secondary inorganic aerosols (SIA, red circle), secondary organic aerosols (SOA,
 1180 green plus), primary organic aerosols (POA, blue x) and black carbon (BC, black dots); **(c)** Size-resolved Particle
 1181 Activation Ratio (SPAR) under supersaturation (SS) of 0.08% observed by the DMA-CCNC, with warmer colors
 1182 corresponding to higher values; **(d)** Probability Density Function (PDF) of growth factor (GF-PDF) at 200 nm
 1183 observed by the HTDMA; **(e)** PDF of shrinkage factor (SF-PDF) at 200 nm and 200 °C observed by the VTDMA;
 1184 **(f)** PDF of lag time at 200 nm observed by the DMA-SP2. The blue, red, and green shaded periods represent the three
 1185 periods with moderate pollution, heavy pollution, and clean conditions, respectively.



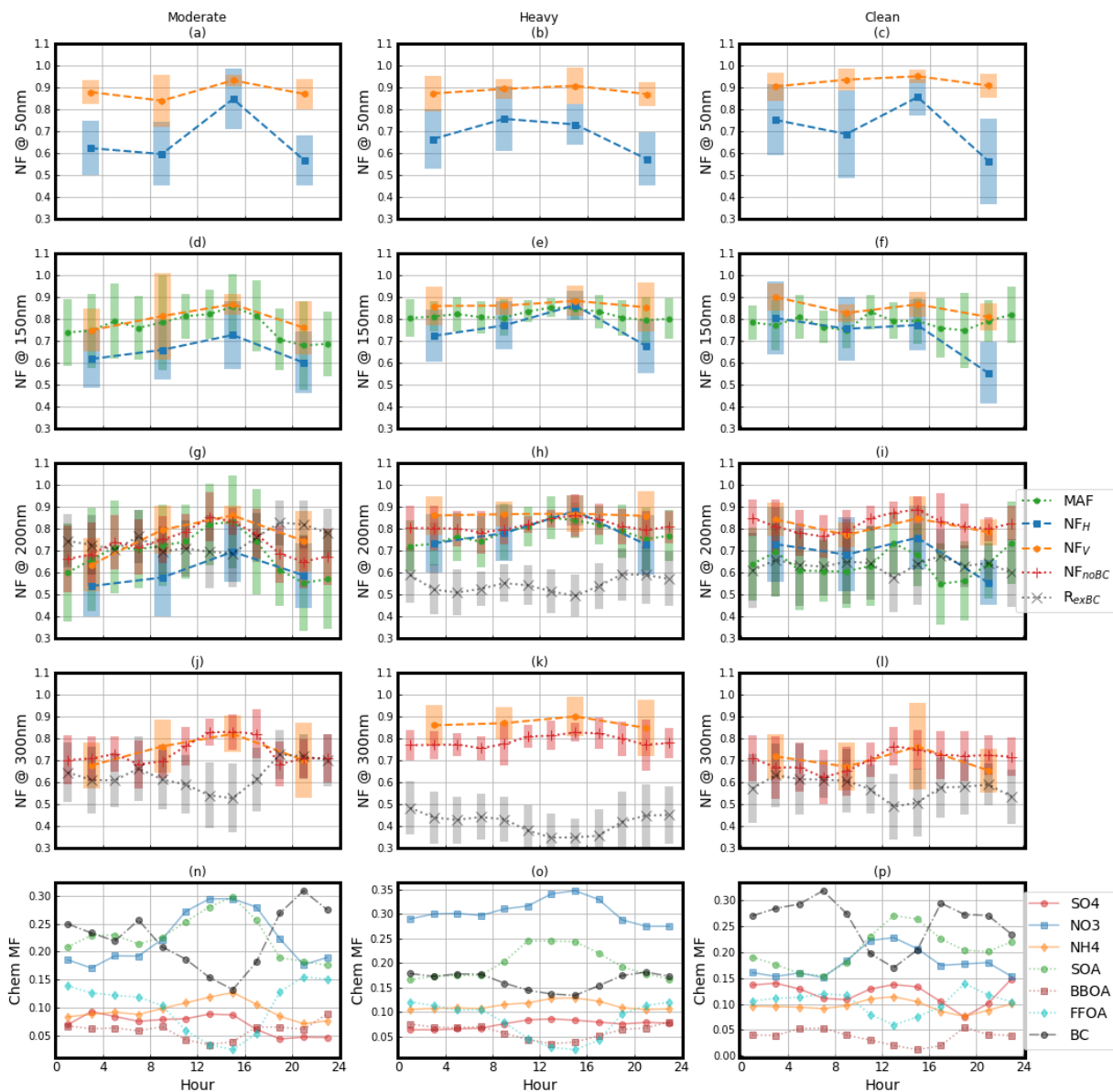
1186

1187 **Figure 2.** The campaign average of (a) Size-resolved Particle Activation Ratio (SPAR) curves measured by DMA-
 1188 CCNC at the three supersaturations (SSs, represented by different colors and markers), (b) Probability Density
 1189 Function (PDF) of lag time measured by DMA-SP2 at four particle sizes (represented by different colors and markers),
 1190 (c) PDF of growth factor (GF) measured by HTDMA at four particle sizes (represented by different colors and
 1191 markers), (d) PDF of shrinkage factor (SF) measured by VTDMA under the temperature of 200 °C at five particle
 1192 sizes (represented by different colors and markers). The shaded areas indicate the standard deviations.



1193

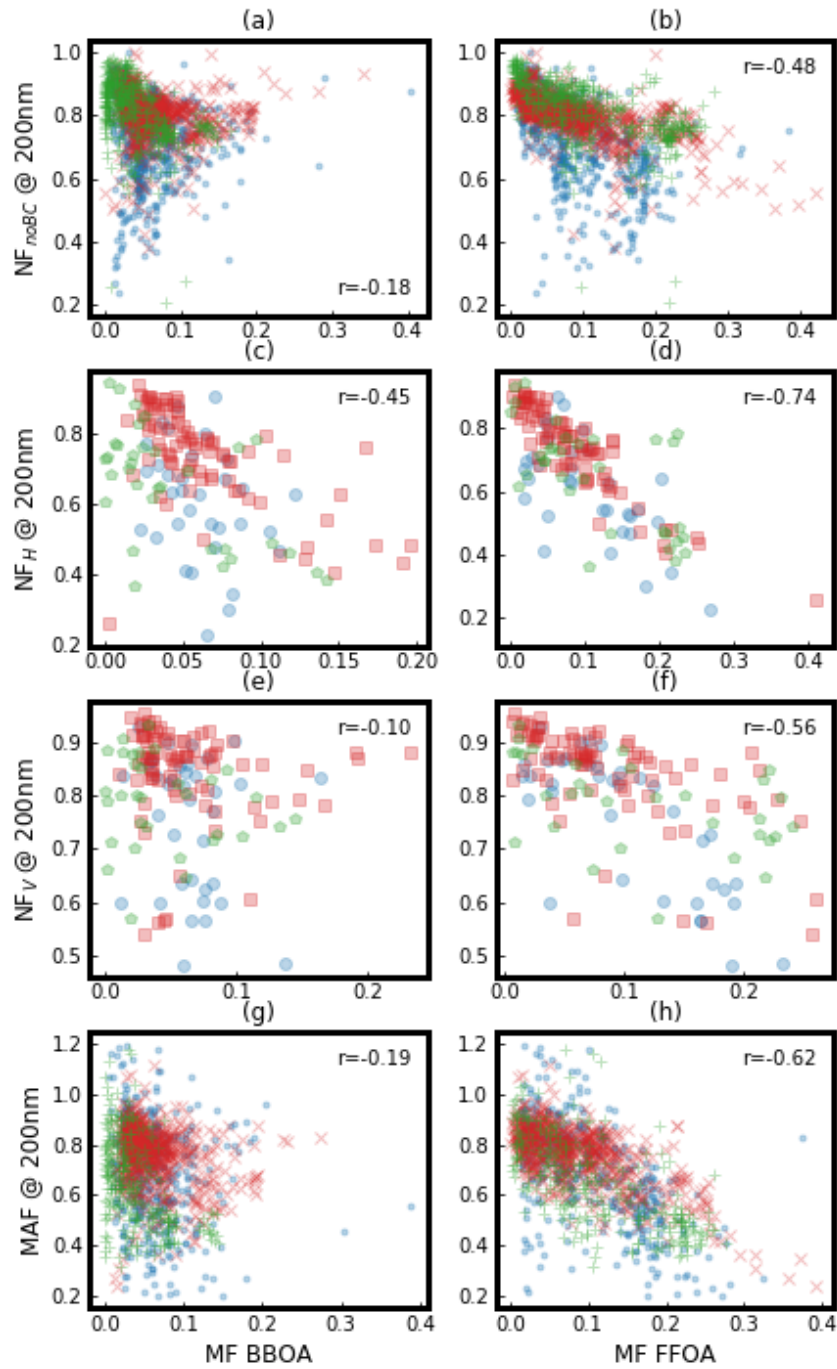
1194 **Figure 3.** (a–c) Size dependence of MAF (green circle), NF_H (blue triangle), NF_V (yellow square), NF_{noBC} (red x),
 1195 and R_{exBC} (black x) during the three periods. **MAF**: Maximum Activation Fraction, an asymptote of the measured
 1196 Size-resolved Particle Activation Ratio (SPAR) curve at large particle size. **NF_H** : Number Fraction of Hydrophilic
 1197 aerosol whose hygroscopicity parameter is higher than ~ 0.07 . **NF_V** : Number Fraction of Volatile aerosol whose Shrink
 1198 Factor at 200 °C is lower than 0.85. **NF_{noBC}** : Number Fraction of black carbon (BC)-free particles. **R_{exBC}** : Number
 1199 fraction of externally mixed BC particles in total BC-containing particles. (d–f) Corresponding mass fractions (MFs)
 1200 of aerosol chemical components (identified by colors) during the three periods, including secondary organic aerosols
 1201 (SOA), biomass burning organic aerosol (BBOA), fossil fuel organic aerosols (FFOA), and inorganic ions including
 1202 sulfate (SO_4), nitrate (NO_3), and ammonium (NH_4).



1203

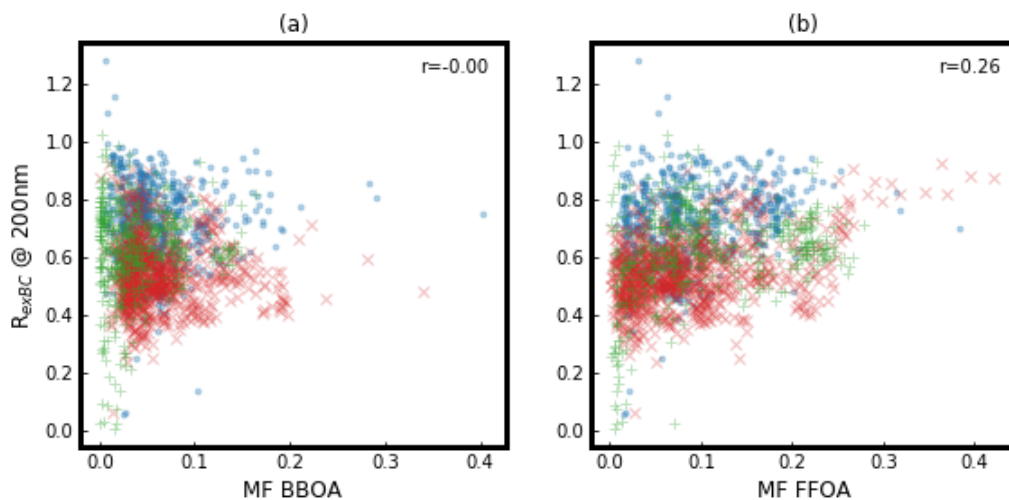
1204 **Figure 4. (a–l)** Diurnal variations of aerosol mixing state parameters (identified by color and marker) at different
 1205 particle sizes (50, 150, 200, and 300 nm) during the three periods. The shaded areas indicate the standard deviations.
 1206 **(m–o)** Diurnal variations of mass fractions (MFs) of aerosol chemical components, including secondary organic
 1207 aerosols (SOA), biomass burning organic aerosol (BBOA), fossil fuel organic aerosols (FFOA), and inorganic ions
 1208 including sulfate (SO₄), nitrate (NO₃), and ammonium (NH₄) (identified by color and marker) during the three periods.

1209



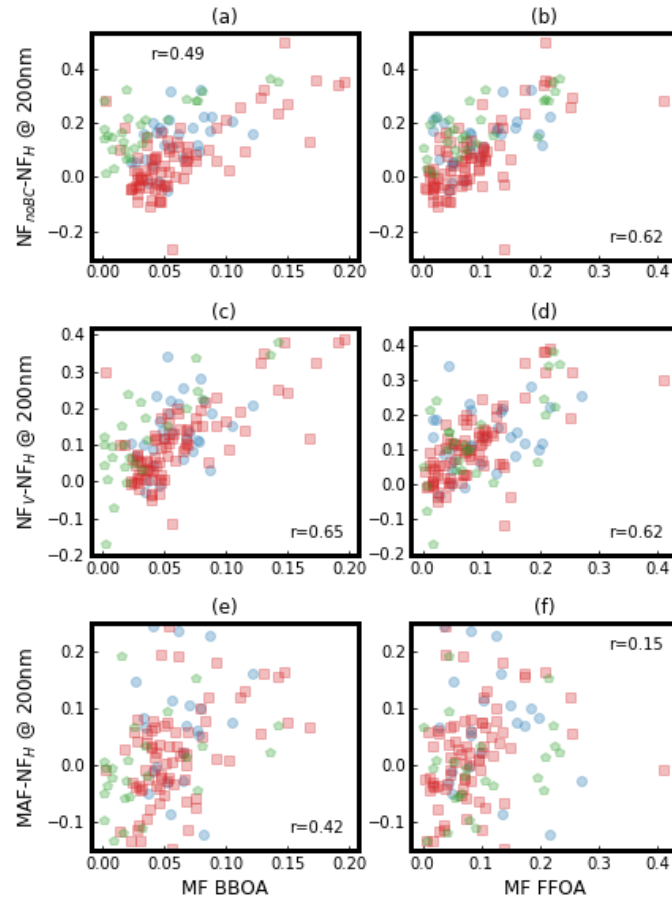
1210

1211 **Figure 5.** The correlations between aerosol mixing state parameters and mass fractions (MFs) of biomass burning
 1212 organic aerosol (BBOA) and fossil fuel organic aerosols (FFOA) during different periods (moderately polluted period:
 1213 blue dot or circle; heavily polluted period: red x or square; clean period: green plus or pentagon), with r representing
 1214 the correlation coefficient.



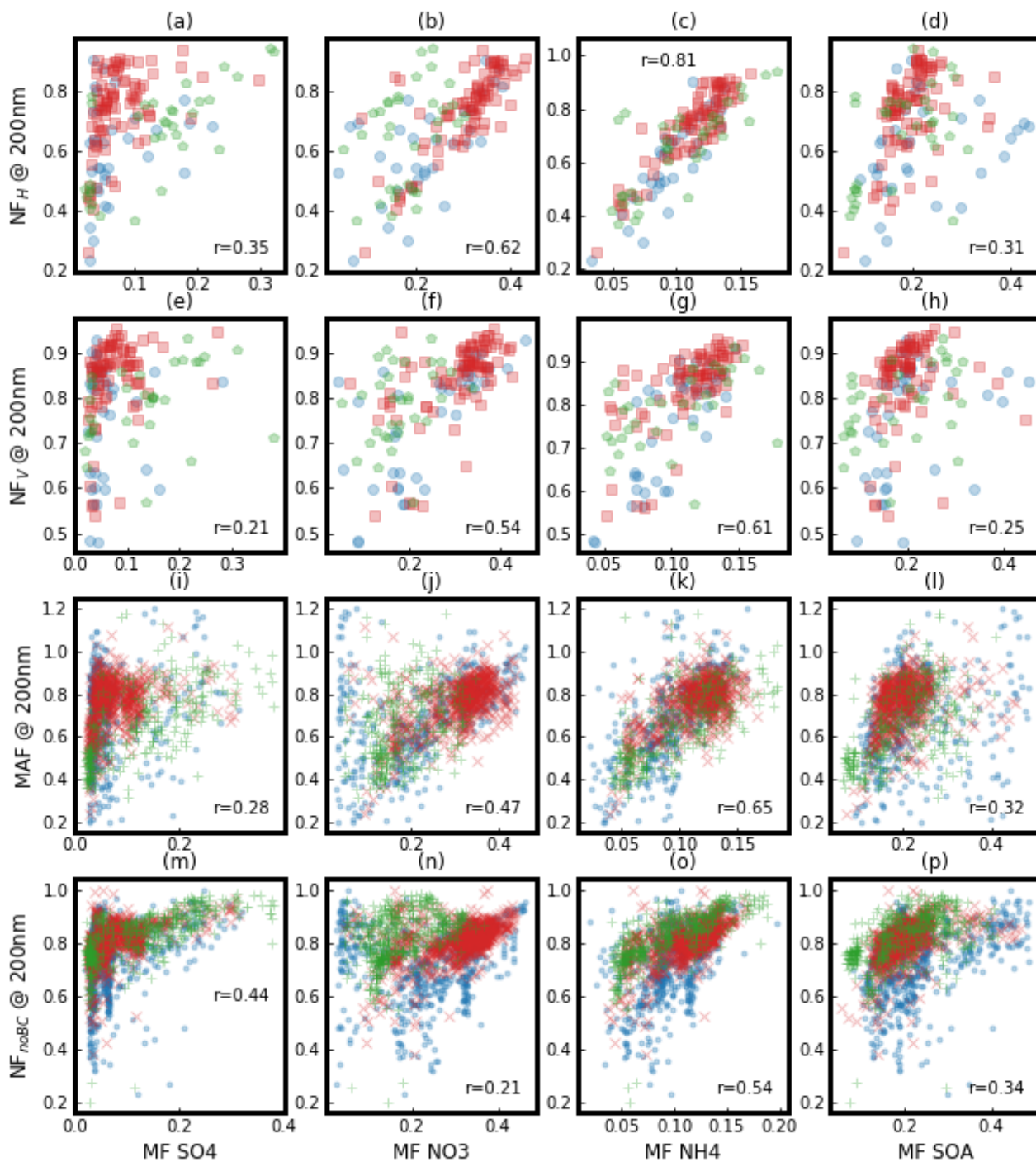
1215

1216 **Figure 6.** The correlations between the ratio of externally mixed black carbon (BC) in total BC particles (R_{exBC}) and
 1217 mass fractions (MFs) of biomass-burning organic aerosol (**BBOA**) and fossil fuel organic aerosols (**FFOA**) during
 1218 different periods (moderately polluted period: blue dot; heavily polluted period: red x; clean period: green plus), with
 1219 r representing correlation coefficient.



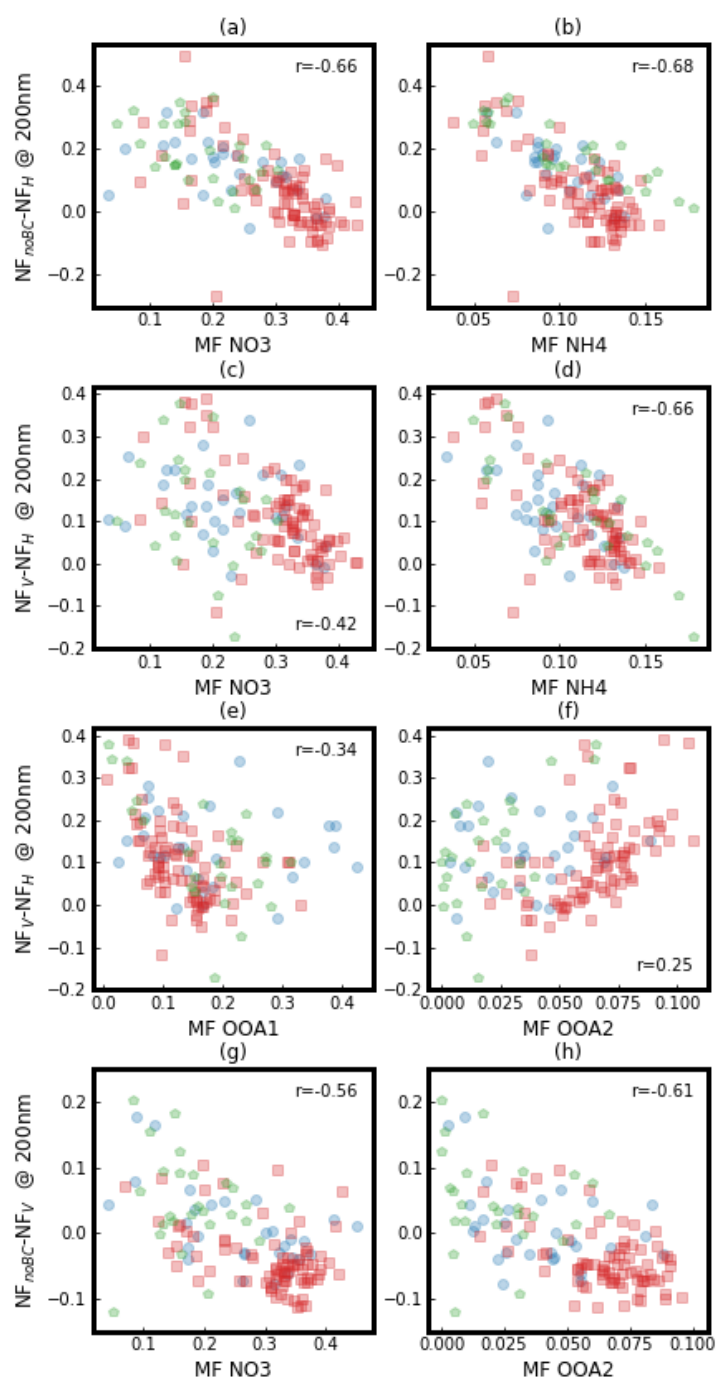
1220

1221 **Figure 7.** The correlations between the difference among the four aerosol mixing state parameters at particle size 200
 1222 nm and mass fractions (MFs) of biomass burning organic aerosol (**BBOA**) and fossil fuel organic aerosols (**FFOA**)
 1223 during different periods (moderately polluted period: blue circle; heavily polluted period: red square; clean period:
 1224 green pentagon), with r representing correlation coefficient.



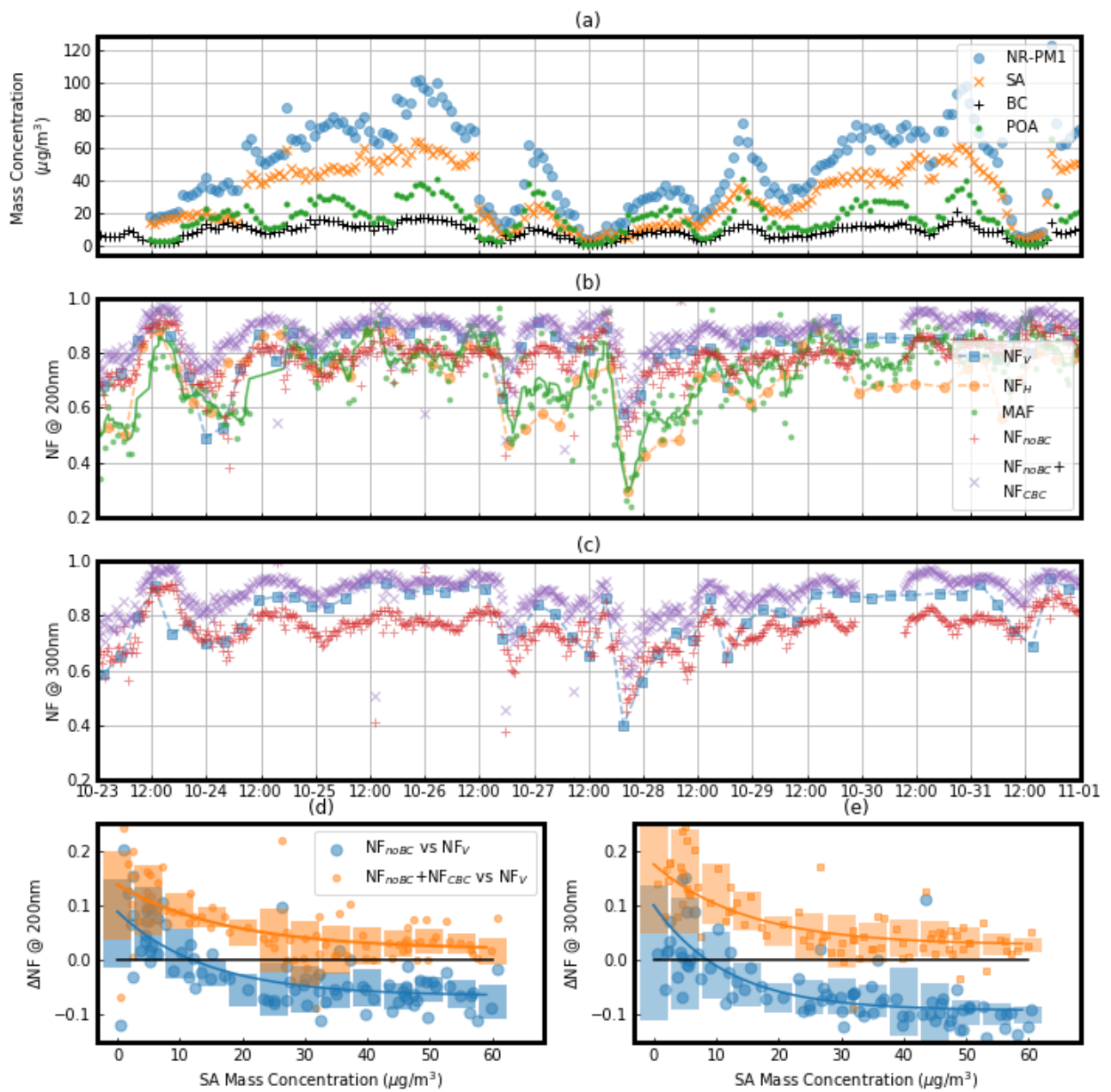
1225

1226 **Figure 8.** The correlation between the four aerosol mixing state parameters and mass fraction (MF) of secondary
 1227 aerosol (SA) components during different periods (moderately polluted period: blue dot or circle; heavily polluted
 1228 period: red x or square; clean period: green plus or pentagon), with r representing correlation coefficient. SA
 1229 components include secondary organic aerosols (SOA), sulfate (SO₄), nitrate (NO₃), and ammonium (NH₄)



1230

1231 **Figure 9.** The correlation between the difference among the four aerosol mixing state parameters and mass fraction
 1232 (MF) of secondary aerosol (SA) chemical components during different periods. OOA1 and OOA2 are two secondary
 1233 organic aerosol (SOA) factors resolved from aerosol mass spectrometer (AMS) measurements using the Positive
 1234 Matrix Factorization (PMF) technique. Moderately polluted period: blue circle; heavily polluted period: red square;
 1235 clean period: green pentagon.



1236

1237 **Figure 10.** Variations of different aerosol mixing state parameters during the pollution accumulation process. (a) The
 1238 time series of mass concentrations of non-refractory PM_{10} (NR- PM_{10}), secondary aerosols (SAs) (including inorganic
 1239 ions and secondary organic aerosols (SOA)), primary organic aerosols (POA) and black carbon (BC) (identified by
 1240 colors and markers). (b and c) The variations of different aerosol mixing state parameters (identified by colors and
 1241 markers) at particle size 200 nm (b) and 300 nm (c). (d and e) The variations of the difference between NF_V and
 1242 NF_{noBC} ($\text{NF}_V - \text{NF}_{noBC}$, blue large circle) and the difference between NF_V and $\text{NF}_{noBC} + \text{NF}_{CBC}$ ($\text{NF}_V - (\text{NF}_{noBC} + \text{NF}_{CBC})$,
 1243 yellow small circle) with the mass concentration of SA at particle size 200 nm (d) and 300 nm (e) NF_{CBC} : Number
 1244 Fraction of thickly coated black carbon (BC) particles.

1245